Original Paper

Formation mechanism of fault accommodation zones under combined stress in graben basin: Implications from geomechanical modeling

Qi-Qiang Ren [a], Jin-Liang Gao [b, *], Rong-Tao Jiang [c], Jin Wang [d], Meng-Ping Li [e], Jian-Wei Feng [f]

[a] Institute of Sedimentary Geology, Chengdu University of Technology, Chengdu 610059, Sichuan, China
[b] PetroChina Research Institute of Petroleum Exploration and Development, Beijing, 100083, China
[c] Jianghan Oilfield Oil and Gas Production Capacity Construction Management Center, Chongqing, 408000, China
[d] Sinopec Chongqing Fuling Shale Gas Exploration and Development Company, Chongqing, 408000, China
[e] College of Energy, Chengdu University of Technology, Chengdu 610059, Sichuan, China
[f] School of Geoscience, China University of Petroleum (East China), Qingdao 266580, Shandong, China

ARTICLE INFO

ABSTRACT

A fault accommodation zone is a type of structure that is defined as regulating displacement and strain between faults structure. Increasing numbers of fault accommodation zones are being identified in graben basins, indicating the potential exploration target and petroleum accumulation areas. This study aims to analyze the formation mechanism and development of fault accommodation zones under combined stress by a numerical simulation method considering geomechanical modeling. Using three-dimensional (3-D) seismic interpretation and fractal dimension method, exampled with the Dongxin fault zone, the fault activity and fault combination pattern were conducted to quantitatively characterize the activity difference in fault accommodation zones. Combined with mechanical experiment test, a geomehcanical model was established for fault accommodation zones in a graben basin. Integrating the paleostress numerical simulations and structural physical simulation experiment, the developmental characteristics and genetic mechanism of fault accommodation zones were summarized. Influenced by multi movements and combined stresses, three significant tectonic evolution stages of the Dongxing Fault Zone (DXFZ) were distinguished: During the E_s^3 sedimentary period, the large difference in the stress, strain, and rupture distribution in various faults were significant, and this stage was the key generation period for the prototype of the DXFZ, including the FAZ between large-scale faults. During the E_s^2 sedimentary period, the EW-trending symmetric with opposite dipping normal faults and the NE-SW trending faults with large scale were furtherly developed. The junction area of two secondary normal faults were prone to be ruptured, performing significant period for inheriting and developing characteristics of fault accommodation zones. During the E_s^1 sedimentary period, the high-order faults in the DXFZ exhibited the obvious fault depressions and strike-slip activity, and the fault accommodation zones were furtherly inherited and developed. This stage was the molded and formative period of the FAZ, the low-order faults, and the depression in the DXFZ.

1. Introduction

A fault accommodation zone (FAZ) is defined as a structure that is generated to regulate lateral normal faults and the deformation and displacement between them, characterized with the overlapping of lateral normal faults and directly transferred strain between the overlapping normal faults (Gibbs, 1984; Morley, 1988). Referenced by the transfer zone proposed in 1969 and modified in 1984 in the study of the structural system (Dahlstrom, 1969; Gibbs, 1984), the FAZ was widely existed in the crustal structural system, performing the role of regulating the displacement conversion between major faults (Bosworth, 1985; Morley et al., 1990; Faulds and Varga, 1998; Fossen and Rotevatn, 2016). In graben basin, the strike and geometry of the main structure were significantly

influenced by the FAZ, affecting the distribution of water systems and sedimentary systems, indicating the great significance to petroleum geology (Chorowicz and Benissa, 2016; Wang et al., 2016; Liu et al., 2022). Two significant types of deformation or displacement between normal faults were distinguished, the hard linkage and the soft linkage (Walsh and Watterson, 1991; Peacock and Sanderson, 1994; Conti et al., 2017; Henaish, 2018). The hard linkage was represented by the normal faults, and the soft linkage was characterized with the relay ramps in the overlapping normal faults (Moustafa, 2002; Soliva and Benedicto, 2004; Moustafa and Khalil, 2017; Peiro et al., 2020). The accommodation zones were structures accommodating strain and stress between overlapping faults, and transfer faults were faults allowing kinematic linkages between other major faults and showing a large intersection angle with these faults (Bosworth, 1987; Peacock et al., 2000; Ze and Alves, 2019). Explanatorily, the faults of transfer zones were active at the same time, but the faults of accommodation zones were not necessary to be active at the same time (Bosworth, 1985; Peacock et al., 2000). Since 1990s, the research on accommodation zones has obtained increasing attention by many scholars. The accommodation zone and transfer zone could be used interchangeably in many studies (Faulds and Varga, 1998; Wang et al., 2022). Confirmed through exploration in the Bohai Bay Basin, Subei Basin, and other oil-gas fields, the theoretical research on oil- and gas-bearing graben basins has achieved significant process (Faulds and Varga, 1998; Moustafa and Khalil, 2017; Wang et al., 2022; Liu et al., 2022). A FAZ, characterized with significant structure to regulate the conservation of regional extension or shortening during the basin deformation, performing key roles in basin evolution and subsequent basin transformation (Bellahsen et al., 2013; Mart et al., 2018). Especially, the development of petroleum source rocks, the sedimentary distribution, the formation of structural traps, and channels of oil-gas migration were significantly controlled and influenced by accommodation zones (Tong et al., 2015; Tian et al., 2016; Chorowicz and Benissa, 2016; Wang et al., 2016; Liu et al., 2022).

Constrained by the relative inclination relationship of the faults on the section, two important categories of accommodation zones were divided, the same direction type and the reverse type (or conjugate type) (Morley et al., 1990; Gawthorpe and Hurst, 1993; Ma et al., 2019). Based on the geometric structures, the reverse type representing the transformation structure formed between two normal faults with opposite inclinations was divided into the back type (or divergent type) and the opposite type (or convergent type) (McClay et al., 2002; Fossen, 2016; Bose and Mitra, 2014). Constrained by the mutual distribution relationship of faults on the plane and the genetic mechanism, transformation structures could be divided into four types: approach type, overlap type, parallel type, and collinear type (Bose and Mitra, 2010; Wang et al., 2013; Bellahsen et al., 2013; Paul and Mitra, 2013). The strata rotation angles in different stages and the vertical expansion index were conducted to quantitatively characterize the degree of deformation of the accommodation zone in the horizontal extension and vertical direction, respectively (Peacock and Sanderson, 1994; Ferrill and Morris, 2001). However, there are no clear parameters to characterize the deformation and activity of the accommodation zones from the two-dimensional (2-D) or three-dimensional (3-D) aspect. The genetic mechanism of a FAC could be effectively analyzed by the physical experimental models (PEM) (Corti et al., 2002; Konstantinovskaya et al., 2007; Tong et al., 2015; Liu et al., 2022). Additionally, the reservoir fracture prediction and in-situ stress field were effectively and quantitatively simulated through the geomechanical models (Jiu et al., 2013; Liu et al., 2017, 2022; Guo et al., 2019; Ren et al., 2019, 2020). During the numerical simulation, the stress and strain fields of the paleo and current tectonic

stages could be obtained, providing the possibility to directly analyze the genetic mechanism of accommodation zones. It is more likely to become the novel trend to characterize the genetic mechanism of accommodation zones by integrating the PEM and the finite element numerical simulation.

In this manuscript, aiming at analyzing the genetic mechanism and development characteristics of accommodation zones under combined stress, the Dongying Sag, a typical graben basin, was selected to study the fault activity parameters and intensity. Through three-dimensional (3-D) seismic interpretation and fractal dimension method, the fault activity and combination pattern were used to quantitatively characterize the activity difference. Based on the mechanical experiment test, the tectonic evolution and genetic mechanism of accommodation zones were analyzed by establishing a geomechanical model. Additionally, the geometry, kinematics, and dynamics characteristics of FAZs in the graben basin were also summarized. This study results could provide a novel way to analyze the formation mechanisms of accommodation zones and guide the exploring of oil and gas reservoirs in graben basins.

2. Geological setting

The Dongying Sag, located at the southeast of Bohai Bay Basin in Eastern China (Fig. 1a), was characterized with a major depression of an approximately 5700 km^2 area, exhibiting half graben rift-down basin (Chen et al., 2009; Cao et al., 2014; Wang et al., 2016; Zhang et al., 2019). The north of Dongying Sag is bounded to the Guangrao bulge area, and the west of Dongying Sag is bounded to the Qingcheng bulge and Binxian bulge area. Additionally, the south and east of Dongying Sag is bounded to the Chenjiazhuang bulge area and Kendongqingtuozi bulge area, respectively (Fig. 1b). On the plane, seven secondary structural units in the Dongying Sag was subdivided, the northern steep slope zone (NSTZ), the central uplift zone (CUZ), the southern gentle slope zone (SGSZ), Lijin sub-sag, Niuzhuang sub-sag, Boxing subsag, and Minfeng sub-sag (Zhang et al., 2014; Wang et al., 2020).

The study area (Dongxin area), located at the eastern section of the CUZ, was composed of five nearly EW strike secondary faults, namely Ying 1, Ying 31, Ying 8, Xin 1, and Xin 120 (Fig. 1c). The main framework of the Dongxin fault zone (DXFZ) was composed of the above mentioned five faults, controlling the structural framework and sedimentary system of the study area (Yang et al., 2017; Lu et al., 2019). Morphologically, the DXFZ was characterized with narrow in the west and wide in the east. The DXFZ started from the western end of the Ying 1 fault in the west, and reached the eastern end of the Xinzhen parallel fault system in the east. The north and south of the DXFZ was Ying 8 fault and Xin 133 fault, respectively (Fig. 1c) (Lu et al., 2019). Constrained by the changeable shape and combination of faults, various transformation slopes and regulating faults were developed between different faults, at the bend and fault tip of a single fault. Three formations of the Paleogene in the study area could be distinguished from bottom to top, the Kongdian (E$_k$), Shahejie (E$_s$), and Dongying (E$_d$) Formations (Fig. 2, Xu et al., 2018). Furtherly, four Sections of the Shahejie Formation could be subdivided from bottom to top, the Fourth Section (E$_s^4$), the Third Section (E$_s^3$), the Second Section (E$_s^2$), and the First Section (E$_s^1$). Characterized with self-generation and self-storage, the Shahejie Formation performed as a good reservoir, indicating the thick oil layer (Fig. 2) (Zhang et al., 2010; Zahid et al., 2016; Xian et al., 2018).

Through the numerous studies on the DXFZ, six significant tectonic evolution processes were identified, E$_k$—E$_s^4$, Early-Middle E$_s^3$, Late E$_s^3$, E$_s^2$, E$_s^1$, and E$_d$—N$_m$ (Minghuazhen Formation) sedimentary periods (Wu et al., 2012; Li et al., 2014). During the stage I (E$_k$—E$_s^4$), influenced by the NS extension, the DXFZ was initially composed of Ying 8, Ying 1, and Ying 31 detachment fault system,
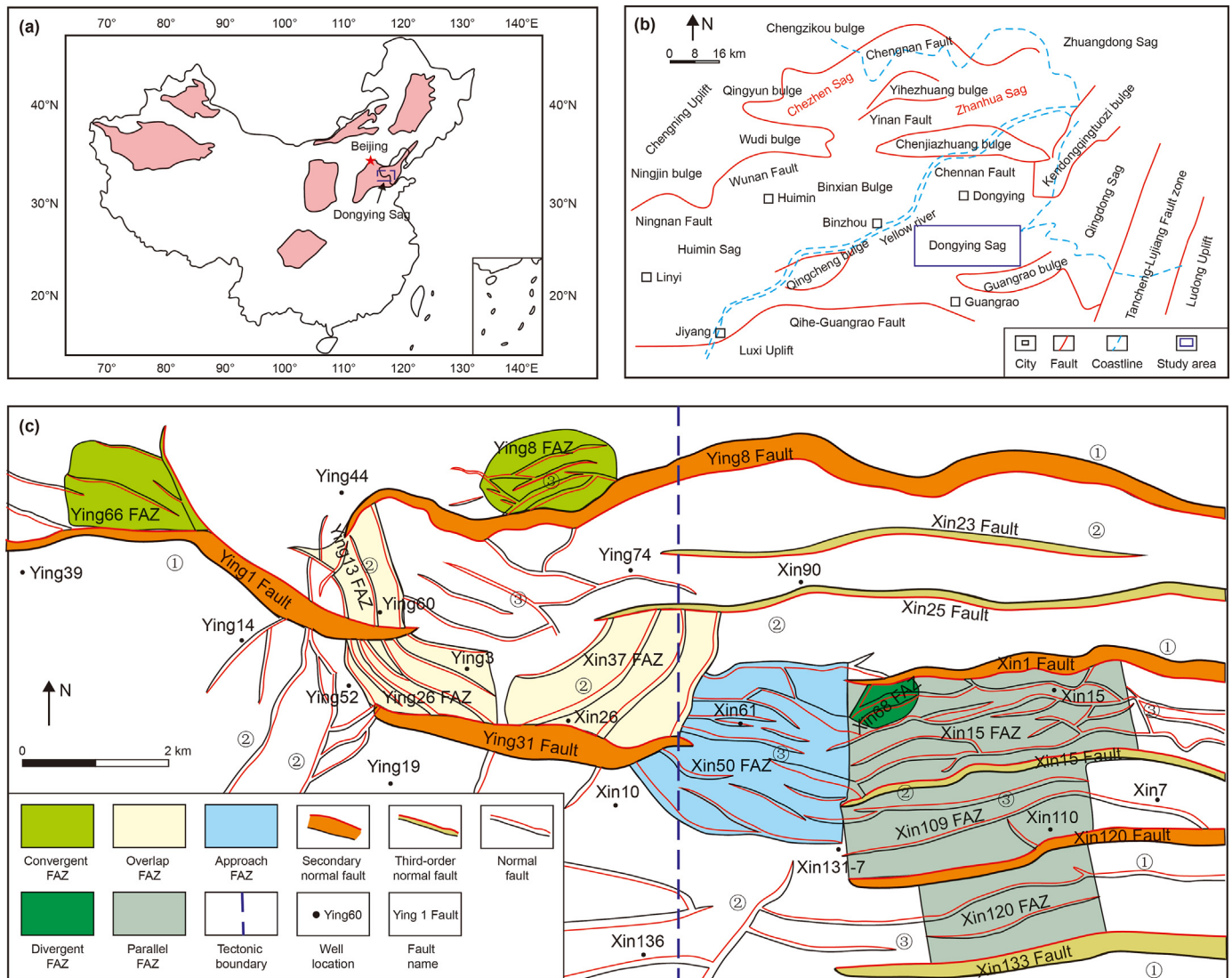
Fig. 1. Location and structural characteristics of the study area. (a) is the map of China; (b) shows the tectonic location map of study area; (c) is the structural features of Dongxin fault zone, where FAZ is fault accommodation zone. In the figure: ① is the E_s^4 Formation sedimentary period; ② shows the E_s^3 Formation sedimentary period; ③ refers to the E_s^2-E_s^1 Formation sedimentary period.

indicating the early development stage of Dongying Sag (Wu et al., 2012; Lu et al., 2013). For the stage II (Early-Middle E_s^3), constrained by reverse traction, a series of anticlines were formed in the earlier detachment fault system (Yuan et al., 2013; Lu et al., 2019). During the stage III (Late E_s^3), influenced by dextral strike-slip action of the Tanlu fault zone, the extensional and torsional faults were developed and superimposed on the early extensional faults, then the basic framework of the DXFZ was formed (Wang et al., 2004; Li et al., 2014). For the stage IV (E_s^2), constrained by differential compaction effects, the plastic rock layer of E_k and E_s^4 Formation occurred diapir upwelling, complicating the existing faults, then the development of DXFZ was basically completed (Wu et al., 2012; Zhao et al., 2014). During the stage V (E_s^1), the composite action of extensive torsion and diapir upwelling was developed continuously, indicating similar fault patterns with the E_s^2 sedimentary period (Yuan et al., 2013; Lu et al., 2019). For the stage VI (E_d—N_m), the tectonic activity began to weaken and gradually stooped. Additionally, the complex fault pattern was also transferred to be simple, until the main fault completely disappeared at the top of the N_m (Li et al., 2014; Xian et al., 2018; Wang et al., 2020). The FAZ,

product used to regulate tectonic deformation, indicating the consistent evolutionary features with the DXFZ. The activity of FAZ was mostly reached the peak during the stage III—IV, and the FAZ was eventually established during the stage V (Tian et al., 2012; Lu et al., 2019). On a larger scale, as a significant fault zone in the Dongying Sag, the orientation of DXFZ may be not random, especially under the combined stress of extensive torsion and diapir action. Studying the genetic mechanism of the FAZ not only has significance for the genesis and evolution of the DXFZ, but also provides guidance for the exploration and development of oil and gas in the study area.

3. Methods and techniques

3.1. 3-D seismic interpretation

To study the developmental characteristics of DXFZ, the high-precision 3-D seismic interpretation was conduct to analyze structural combinational patterns vertically and horizontally (Fig. 3a). Two key methods were used to make a fine seismic

Erathem	System	Formation	Code	Thickness	Stratigraphy	Lithology	Oil layer	Reservoir	Typical oil field	Cap rock	Oil-forming combination
Cenozoic	Quanternary	Pingyuan	Q	250–350		Yellow and grey clay with silty sand					
	Neogene	Minghuazhen	N_2m	100–120		Brown-yellow, brown-red mudstone with siltstone				▥	Lower generation and upper storage
		Guantao	N_1g	300–400		Interbed of fuchsia, grey-green mudstone and siltstone		○●○	Caoqiao Linfanjia		
		Dongying	E_3d	100–800		Unequal thickness interbed of gray mudstone and sandstone			Shengtuo		
	Paleogene	Shahejie section I	$E_{3s}{}^1$	0–450		Grey mudstone mixed with sandstone, biological limestone, dolomite			Jinjia Caoqiao Linfanjia	▥	
		Shahejie section II	$E_{2-3s}{}^2$	0–350		Red, grey mudstone and sandstone interbed with carbonaceous shale			Shengtuo Dongxin		Self-storage
		Shahejie section III	$E_{2s}{}^3$	700–1200		Interbed of grey mudstone and sandstone, dolomite, few carbonaceous shale			Liangjialou Dongxin Xianhezhuang		
		Shahejie section IV	$E_{2s}{}^4$	1500		Fuchsia, grey-green mudstone with sandstone and thin limestone			Yonganzhen		
		Kongdian upper section	E_{1-2k}			Fuchsia sandstone and mudstone interbed			Pingfangwang		Upper generation and lower storage
		Kongdian lower section				Grey mudstone with sandstone					
Mesozoic	Upper Jurassic-Upper Cretaceous		J_1-K_2	200–500		Mud-sandstone with basic volcanic rocks			Gaoqing		Young source in old reservoir
	Middle and Lower Jurassic		J_{1+2}			Interbed of mudstone and sandstone					
Paleozoic	Lower Permian		P_1	100–200		Mudstone, sandstone with coal layer					Young source in old reservoir
	Upper Carboniferous		C_{2+}	200–250		Mudstone, sandstone with coal layer			Gaoqiao		
	Middle and Lower Ordovician		O_{1+2}	400–800		Dolomite, breccia, massive limestone, leopard limestone					
	Cambrian		$\in$	600–800		Fuchsia shale with dolomite, oolitic, pimple, and bamboo leaf limestone					

Fig. 2. Strata, stratigraphic profile, lithology, oil layer, and reservoir characteristics in the Dongying Sag (Xu et al., 2018, modified).

characterization, the experienced manual interpretation and superimposed ant body tracking. Constrained by the logging and drilling data from typical wells in the DXFZ, we completed the 3-D seismic interpretation in the study area. The experienced manual interpretation was mainly used to conduct fine characterization of fault profile styles and detailed characterization of planar features. The superimposed ant body tracking was primarily used to analyze the fault combination patterns in the plane. Based on the well logging data, the stratigraphic stratification scheme was clarified, then the structural maps of different horizons were obtained.

3.2. Fault activity analysis and fractal dimension method

In this manuscript, fault growth index method was used to quantitatively analyze the activity of the normal faults by the fault throw and activity parameters. Then the activity of faults was characterized by the activity parameters in map view. Basically, the fault activity intensity showed distribution difference in various tectonic periods and layers (Fig. 3b). Additionally, in order to study the growth fault activity, the fault throw was necessary to be calculated during each significant geological period (Whittaker and Walker, 2015; Liu et al., 2018). Aiming at determining the fault throw of a growth fault during a certain period, the thickness difference was calculated between two sedimentary strata. Based on the 3-D seismic interpretation, the strata thickness was obtained by integrating the fault occurrence and seismic section orientation. Constrained by the combined stress of extensive torsion and diapir upwelling, the DXFZ was characterized with strike-slip, normal,
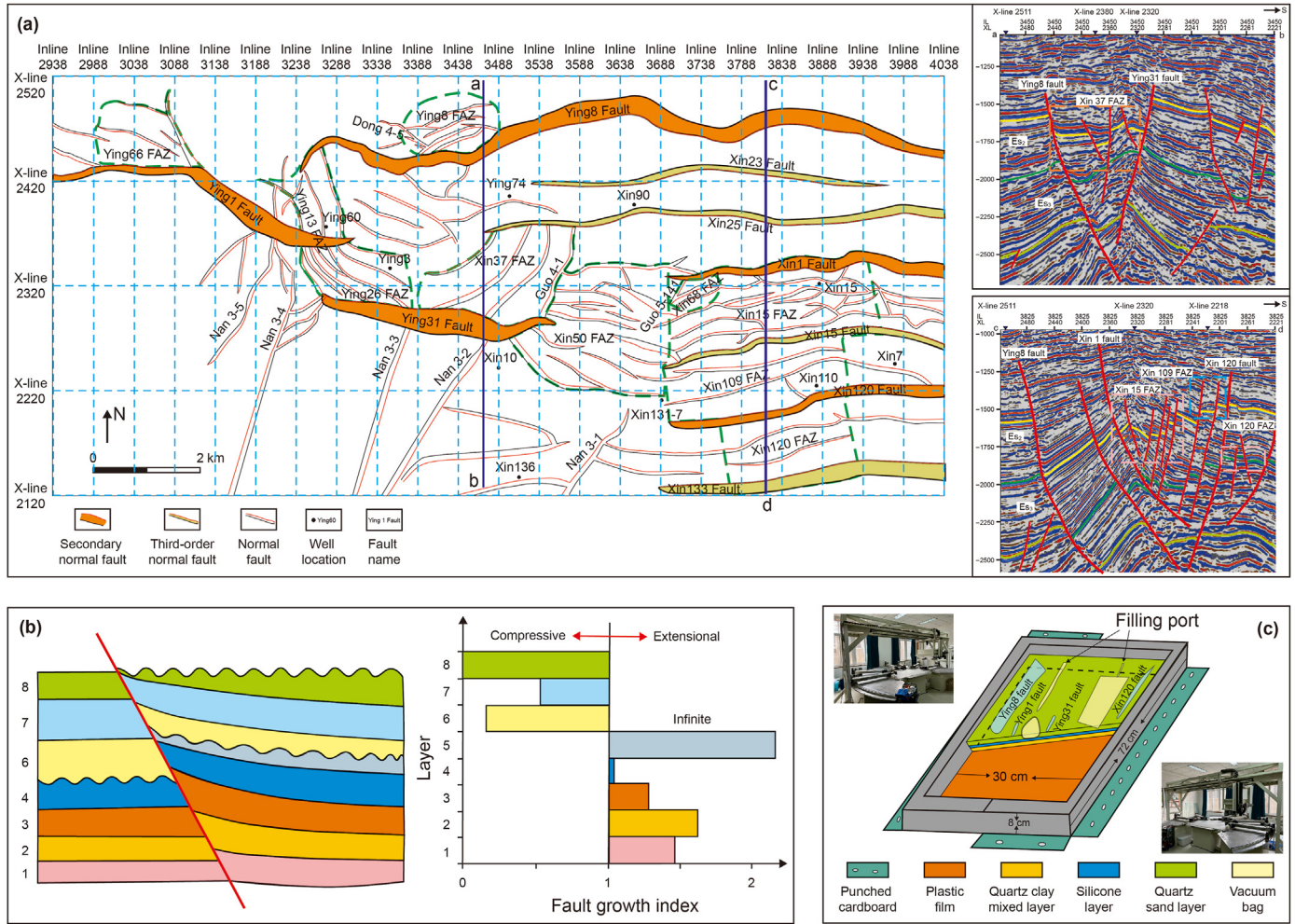
Fig. 3. (a) 3-D spatial characteristics of Dongxin fault zone and seismic lines; (b) principle schematic diagram of fault growth index; (c) schematic diagram of the physical simulation experimental model.

and reverse fault properties, and the obtained fault throw could be used to analyze the fault activity intensity. To obtain the activity intensity of various scale and complex combinational style faults, Eq. (1) was conducted to quantitatively calculate the segmentation of fault activity intensity on a plane (Fu and Yang, 2013; Hu et al., 2016; Wang et al., 2020):

$$G_i = T_{HW}/T_{FW} \tag{1}$$

where G_i is the activity intensity of the active fault, dimensionless; T_{HW} refers to thickness of hanging wall in the corresponding sedimentary period, m; T_{FW} shows thickness of footwall in the corresponding sedimentary period, m; when $G_i > 1$, the tectonic background was interpreted as tensile stress environment, indicating normal faulting activity; when $G_i < 1$, it was interpreted as compressive tectonic stress environment, indicating reverse faulting activity (Chu et al., 2023); when $G_i = 1$, it revealed relatively static rupture activity. Through analyzing deposition rate and improving the contrast accuracy of strata on two sides of the fault, the activity intensity and history of the growth fault could be quantitatively calculated. The magnitude of G_i was also used to indicate the degree of fault activity intensity.

The fractal dimension was used to characterize the complexity and irregularity of various scale faults and quantitatively describe the self-similarity of faults. For the Dongxin study area, the box

fractal calculation technology was adopted to characterize the geometric characteristics of fault structures. During the fractal dimension method process, the square grids with different side lengths were used to describe the plane geometry of a fault in different periods. Then the number of squares in the same level filled by the fault was counted, and the fractal value of each fault could be calculated by Eq. (2) (Ding et al., 2020):

$$D = -\lim_{u \to 0} \lg N(a)/\lg a \tag{2}$$

where D is the fractal dimension value; $N(a)$ refers to the number of squares in the same level filled by the fault, number; a is the side length of square grids, m. Specifically, on the double logarithmic coordinate graph with a (abscissa) and $N(a)$ (ordinate), the least squares method was conducted to fit the slope of the straight line, indicating the desired fractal dimension value D. In this manuscript, constrained by the identification accuracy of seismic data and developmental characteristics of typical faults, total 45 faults with different scales in the study area were measured by the square grids with 1−20 km, respectively (Fig. 3a). Then the correlation between NE-SW strike faults and nearly EW strike faults were analyzed based on the distribution characteristics of fractal dimension values. Furthermore, the relative activity intensity and history of DXFZ was determined.

Emphatically, in order to analyze the formation mechanism of fault accommodation zones under combined stress in graben basin, parameters of fault activity and fractal dimension were conducted to characterize the complexity and irregularity of these faults. Then the formation order of different system faults was precisely determined. The obtained parameters and results could provide guidance for the physical and geomechhanical simulation, and the corresponding geomechanical model of fault accommodation zones could be constructed.

3.3. Rock mechanical testing

Total ten sandstone samples of the Shahejie Formation in the study area were selected to be conduct rock mechanical testing in Qingdao Jiahang Petroleum Technology corporation in Shandong University of Science and Technology. Constrained by the 'International Society of Rock Mechanics Recommended Test Methods' and 'Hydropower Engineering Rock Test Code', the rock mechanical testing was conducted by a TAW-100 triaxial stress testing machine with a test force measurement accuracy of 1.0%. Three key mechanical parameters of specimens were obtained under a normal temperature and pressure, rock's Poisson's ratio, Young's modulus, and compressive strength. The maximum axial stress, maximum confining pressure, minimum confining pressure, the pore pressure, and the temperature were set to 1000 kN, 150 MPa, 5 MPa, and 180 °C. The testing results could provide reliable mechanical parameters for the tectonic physical simulation experiments and finite element numerical simulations, guiding the research on the genetic mechanism of the FAZ.

3.4. Tectonic physical simulation experiment

During the end of Yanshanian movement, the Tanlu fault zone changed from sinistral strike-slip compression to dextral strike-slip tension (Lu et al., 2019). In recent years, frequent earthquakes along the fault zone indicated that the Tanlu fault zone was characterized with strong compression and torsion (sometimes sinistral and sometimes dextral). The controlled depression faults of Cenozoic NNE-NE-trending and NWW-EW trending in Bohai Bay Basin were the result of the superposition of stages of extensional deformation (Tian et al., 2012; Lu et al., 2019). According to the geological background of NNW-SSE extension and local diapir action, the central uplift in Dongying Sag was controlled by the joint action of regional extension and diapir stress (Li et al., 2014; Xian et al., 2018; Wang et al., 2020). During the sedimentary period of Es^3–Es^k Formation, the diapir structure was active, resulting in the formation of DXFZ (Wu et al., 2012; Zhao et al., 2014). During the sedimentary period of Es^2 Formation, the salt plastic strata (Es^4–Es^k) began to arch up the diapir. During the sedimentary period of Es^1 Formation, the recombination action of tensile torsion and diapiric arch continued to develop (Yuan et al., 2013; Lu et al., 2019). Constrained by similarity principles (geometric, dynamic, and kinematic similarity), the physical properties of experimental materials and model size should maintain a certain ratio with the actual corresponding parameters (Hubbert, 1937; Yan et al., 2016; Zhao et al., 2005). Three significant experimental materials were used in this study, quartz sand, clay, and silica gel. To simulate the brittle overlying rock (physical properties follow the Coulomb-Mohr fracture criterion), the quartz sand was selected in the physical simulation experiment. Then the internal friction angle was set to 31°, and the cohesion was extremely small (Krantz, 1991). The silica gel, characterized with transparent, high-viscosity material, was conducted to simulate plastic deformation of the upper crust. Where the strain rate was low, where there was Newtonian fluid properties, indicating very low yield strength (Ter Borgh et al., 2011). In this

manuscript, 80–120 mesh dry quartz sand was used to simulate the rock dominated by mudstone and sandstone (E_s^4–E_d Formation). The slightly moist mixture of quartz sand (80–120 mesh) and clay was conducted to simulate the underlying compacted rock formation (dominated by mudstone) in the lower part of E_k Formation. The mass fraction ratio of quartz sand, clay, and water was 500/60/1. During room temperature, the silica gel with a viscosity of 1.2×104 Pa·s and a density of 0.96 g/cm^3 was used to simulate the plastic detachment layer dominated by salt gypsum rock (E_k–E_s^4 Formation).

The DXFZ was characterized with a 24 km length from east to west and 9.5 km width from north to south. Constrained by large number and complex structure, the idea of "dividing first and then combining, turning the difficult into the easy" was adopted in this experiment, aiming to better describe the development and distribution of faults. During the experiment, the size of the initial model was set to 720 mm × 300 mm (Fig. 3c). The base plate was horizontal, and the boundary was the plank. A stronger plastic film was laid on the bottom plate, extending outward. The extension parts were glued to the base plate, and then holes were punched in the glued area and the nylon cord were threaded. The distance between the holes was set to 60 mm, and the nylon rope could be adjusted into one strand on one side. Through adjusting the length of a single rope, the stress direction could be controlled, and then the stable and uniform extensive torsion stress could be simulated. To simulate the underlying compaction layer, the slightly wet mixture of quartz sand and clay was evenly spread on the plastic film with a thickness of 20 mm. The smooth cardboard with a friction factor of 0.1 and a thickness of 1 mm was preset in this layer to represent Ying 1, Ying 8, Ying 31, and Xin 120 fault. To reproduce the diapir upwelling of the plastic layer, a rectangular vacuum bag (length: 340 mm, width: 55 mm, maximum height difference: 8 mm) and an oval vacuum bag (a-axis: 60 mm, b-axis: 30 mm, maximum height difference: 9 mm) were insert in the silicone layer. Three significant loading stages in the experiment were distinguished, stage I, II, and III. During the stage I, to simulate the right-lateral strike-slip, the stable and continuous EW-direction extension was applied to the northern part of the eastern boundary and the southern part of the western boundary. To simulate the SN-direction extension, the SN-direction tension was loaded to the northern and southern boundaries, respectively. For stage II, the right-lateral strike-slip stress and the NE-direction stretching stress were enlarged, but the SN-direction stretching stress was relatively weakened. During stage III, the right-lateral strike-slip stress and the NE-direction stretching stress were furtherly enhanced, and the NE-direction extension was gradually decreased. Simultaneously, the silicone was slowly injected into the rectangular and oval vacuum bags of the silicone layer.

3.5. Numerical simulation based on geomechanical model

To study the genetic mechanism and development of the FAZ, a 3-D geomechanical model was established by means of finite element method. Constrained by the analyzed fault activity and fractal dimension from seismic interpretation, combined with regional tectonic setting and rock mechanical experimental results, the tectonic experiment simulation and finite element numerical simulation based on geomechanical model were applied to analyze the evolution process of DXFZ. During the process, the deformation and activity of the accommodation zones could be observed and obtained.

Generally, the finite element method was defined as an approximate numerical simulation technique to solve the basic continuous medium problems. During the finite element simulation, the continuous geological body was discretized into many

finite elements, then the numerical solution was obtained (McKinnon, 2001; Hunt et al., 2011; Liu et al., 2017; Ren et al., 2019; Andhumoudine et al., 2021). The discretized finite elements were connected by nodes, and each element could be assigned actual rock mechanic parameters. Three basic variables in the finite element simulation were distinguished, the displacement, stress, and strain. Constrained by the equilibrium conditions and boundary stress of nodes, equations with node displacement (unknown quantity) and overall stiffness matrix (coefficient) were established and solved. Through the interpolation function, the displacement of each node was determined, then the internal stress and strain of each element were furtherly calculated. Consequently, the tectonic stress field could be calculated by combining these units in the whole geological body. The closeness to the actual geological model was significantly related with the number of elements, indicating the simulated accuracy (Islam et al., 2009; Mohammadnejad and Andrade, 2016; Ren et al., 2019, 2021). Five basic operation steps during the finite element simulation were identified, establishing the geological model (Step I), determining the simulated area (Step II), generating the finite element mesh (Step III), determining the action mode of the boundary stress (Step IV), and adjusting the boundary loading conditions (Step V).

During the Step I, the regional area, fault distribution, and lithological categories were distinguished. Combining the 3-D seismic interpretation with the structural evolution, the 3-D geometry of faults with different scales was determined, then the finite element models of faults with different scales were established. For Step II, the studied area considering the effective fault accommodation zone was selected. During the Step III, the continuous geological model was divided into several elements connected by nodes. Then by integrating geological surveys, logging data, and rock mechanical experiment results, the rock mechanical parameters (such as Young's modulus and Poisson's ratio) were assigned to the discretized elements. For the Step IV, through analyzing the structural development characteristics (structural traces and fault activity), the stress direction could be effectively reflected. Then the corresponding geomechanical model was established based on the gathered information. During the Step V, the boundary load conditions including the force on and displacement were set to the corresponding boundary. Through continuously modifying the boundary loading conditions, the simulation results indicated the greatest consistency with the actual geological conditions.

4. Results

4.1. Geometric characteristics of the Dongxin fault zone

The compositions and geometric characteristics of the Dongxin fault zone were complex (Fig. 3a). Four different strike fault groups were distinguished: the nearly EW strike fault, the NE-SW strike fault, the NW-SE strike fault, and the nearly SN strike fault. Among them, the nearly EW-trending and the NE-SW-trending faults were the most significant. Constrained by the combined stress of extensive torsion and diapir upwelling, seven different plane structural styles were identified, linear, arc, echelon, broom-like, oblique, annular, and radial faults. Six significant vertical structural styles were observed, Y-shaped fault, step fault, graben-horst, flower-like structure, salt ridge top graben, and "turtle-back" structures. Through interpreted profiles at different positions, the dip angles and combinational characteristics of faults were changed along different strikes. Constrained by the extensive torsion stress, the northern section of the nearly EW strike faults dipped to the south with a high angle of 55–80°, indicating the characteristics of normal faults. The southern section of the nearly EW strike faults characterized by normal faults, dipped to the north with a high

angle of 60–80° (Fig. 3a). The northern section of the NE-SW trending faults dipped to the southeast with a high angle of 70–85°, revealing the characteristics of normal fault. The southern section of the NE-SW strike faults, characterized by normal faults, dipped to the northwest with a high angle of 65–80°. Additionally, the northern section of the NW-SE strike faults dipped to the southwest with a large angle of 70–80°, indicating the characteristics of normal faults. The southern section of the NW-SE trending faults, characterized by normal faults, dipped to the northeast with a high angle of 50–75°. Constrained by diapir upwelling stress, the northwestern section of the DXFZ was characterized with ring-shaped faults with a high angle of 50–80°.

Especially, due to the complex composition and type among the main faults, the fault accommodation zone (FAZ) with different characteristics were distinguished. According to the combinational pattern of different fault and stress environment, five significant FAZ in the DXFZ were identified, the convergent, overlapping, approaching, divergent, and parallel FAZ (Figs. 1c and 3a). In the southeastern section of DXFZ, three parallel FAZ were determined, Xin 15, Xin 109, and Xin 120 FAZ (Fig. 3a). Constrained by several EW-strike faults with opposite tendency, the Xin 15 and Xin 120 showed the characteristic of reverse FAZ type. The deformation of the main faults was transmitted on both sides along the dip, resulting a larger fault throw in the middle faults. Based on the EW-strike faults with same tendency, Xin 109 was characterized with same direction FAZ type, resulting in step-like faults to collapse to the north in turn. Controlled by the weaker tectonic activities of the rising wall of normal faults, the overlapping FAZ were developed in the overlapping zone in the head and tail between two laterally distributed main faults, such as Ying 13 FAZ, Ying 26 FAZ, and Xin 37 FAZ (Fig. 3a). Combined with the lateral sealing of the fault, the structural trap was formed, exhibiting a higher oil and gas enrichment. The tail end of the Ying 31 fault (Dongying structure) and the heads of the Xin 120, Xin 15, and Xin 1 faults (Xinzhen structure) approached each other in a complex combination pattern (three faults dragged by one fault) at the junction. Then connected by the derived secondary faults, an EW distributed approaching FAZ was formed (Xin 50 FAZ). Constrained by stress release in the inflection and tail ends of faults, the FAZ controlled by a single fault was primarily distributed in the both ends and limbs of the fault zone. The Xin 68 FAZ, performed as a divergent FAZ, was distributed as a shape of "phoenix tail" on the plane, indicating different structural characteristics between the northern and southern parts. The Ying 66 and Ying 8 FAZ, performed as a convergent FAZ, were distributed in the downthrown side of Ying 1 fault and Ying 8 fault, appearing as a slanting target shape on the plane. In this FAZ, one end converged at the turning end of the main fault, and the other end spread outward in a broom-like shape, showing low oil and gas exploration potential. These difference and changes in these characteristics indicated that the activity of the DXFZ was segmented. Basically, the fault trends in the Dongxin area were similar, however, there were significant difference in the fault directions (Fig. 3a). The eastern and western area of the DXFZ was dominated by the EW strike faults, and middle area was dominated by the NW-SE-trending and NE-SW-trending faults.

4.2. Fault activity analysis and fractal dimension

In order to calculate the fault activity in the DXFZ during different periods, the fault growth index method was used in this manuscript. Through characterizing the thickness of hanging wall and footwall, total sixteen growth faults with two significant directions were counted and analyzed. Then the fault activity in various faults with different directions during different periods and segments were determined (Fig. 4a and b). Through splitting the
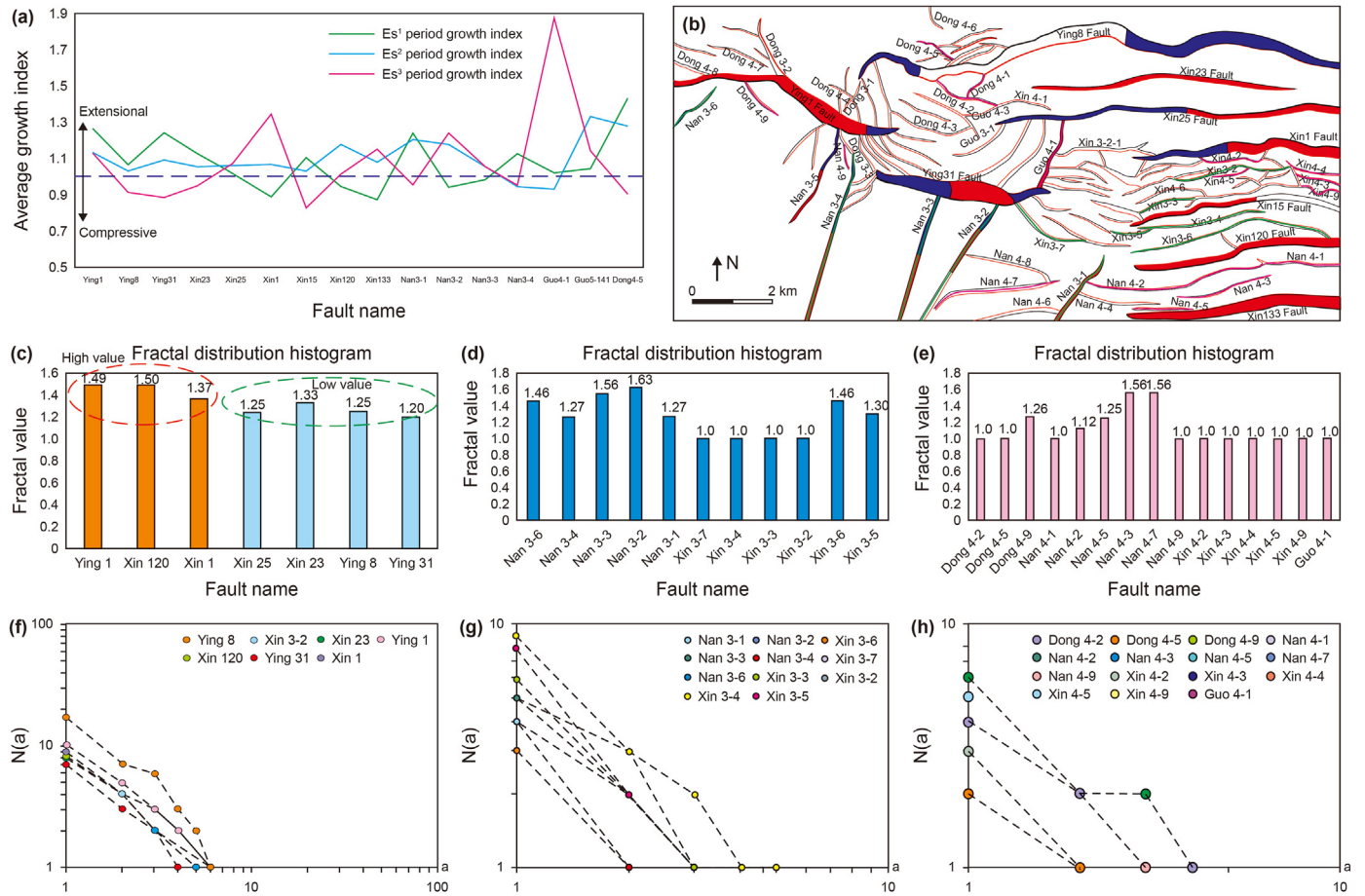
Fig. 4. Schematic diagram of fault activity analysis and fractal dimension results. (a) is fault growth index in different periods with various faults; (b) shows the fault activity characteristics in the plane of E_s^2 period, where red color indicates the value larger than 1, blue color means the value less than 1, and white color shows the value of around 1; (c-e) refer to the fractal value distribution in different faults; (f-h) show the diagram of fractal dimensional calculation of geometric trajectory in various faults.

fault as several segments, the growth index of each segment could be calculated by analyzing the corresponding interpretation profiles (Xia et al., 2018). Then by integrating all the divided segments' results, the average growth index of each fault was obtained through some mathematic methods. The average growth index (activity intensity of fault, could be obtained by Eq. (1)) values of the typical faults were distributed in 0.82 and 1.92, indicating two relatively important periods of tectonic activity. During the periods of $E_s^3–E_s^1$, the experienced tectonic stress environment of Ying 8 and Ying 31 faults gradually evolved from compressive to extensional. The activity of the Xin 23 fault showed a weakening trend, and the activity of the Xin 1 fault gradually moved to the east (Fig. 4a). Especially, the Xin 120 fault only exhibited the activity during the E_s^2 period. During the E_s^1 period, the Ying 1 fault was fully active, indicating strong extensional tectonic activity by the nearly S–N tensile stress. However, only the eastern section of the Ying 1 fault was active during the E_s^3 period, revealing the relatively stable tectonic environment. Through the activity analysis of the E-W strike faults, the fault activity showed characteristics of the east-west segment and north-south subdivision. Additionally, six significant NE-SW strike faults were selected to characterize the fault activity. The average growth index values were primarily concentrated in 0.90–1.92. Most of these faults were active during the periods of $E_s^1–E_s^3$, indicating a high growth index larger than 1.05 (Nan 3–1, Nan 3–2, Nan 3-3, Guo 4–1, Guo 5–141, and Dong 4–5). The high value was distributed in the transition zone (Guo 4–1, 1.92) of Ying 31 fault and Xin 25 fault, indicating a strong

extensional environment. In the southern section of the DXFZ, the activity of NE-SW strike faults was segmented, exhibiting weak activity in the northern segment and strong activity in the southern segment. Consequently, the fault activity of the DXFZ was transmitted from the center to the periphery from the E_s^3 period to the E_s^1 period. Emphatically, the propagation amplitude of the fault activity in the NE-SW direction faults was more obvious than that in the E-W strike faults (Fig. 4b).

Aim at comprehensively study the fault activity, the fractal dimension method was used to analyze the activity difference among faults with different directions and scales. Referenced by the quantitative standards of multiple faults with different scales in the study area (Table 1, Lu et al., 2019, modified), three significant fault sets with different characteristics were distinguished during the fractal dimension research, nearly EW-strike faults with larger extend (6–15 km) length (Type I), NE-SW strike faults with lower extend (1–5 km) length (Type II), and nearly EW-strike faults with medium extend (3–8 km) length (Type III). For Type I, the fractal value was distributed in 1.20 and 1.50, indicating two obvious categories: Ying 1, Xin 120, Xin 1 faults with high fractal values (1.37–1.50), and Xin 25, Ying 8, Xin 23, Ying 31 faults with low fractal values (1.20–1.33). The magnitude of the fractal dimension performed good agreement with the fault activity intensity (Fig. 4a–h). In Type II, the fractal dimension value of the nearly NE-SW trending faults in the DXFZ was between 1.00 and 1.63, showing weak correlation with the nearly N-W strike faults with large extend length (Fig. 4d). Therefore, the nearly NE-SW trending faults

Table 1
The quantitative standards of multiple faults with different scales in the study area.

| Fault level	Cutting depth	Fault scale		Controlling on the oil and gas
		Extend length	Maximum throw	
Primary fault controlling basin	Basement or the upper part of the deep crust	Tens of kilometers to hundreds of kilometers	> 5 km	Control of basin boundaries, sedimentary distribution characteristics, hydrocarbon accumulation and seal combinations, and distribution of the petroleum system
Secondary fault controlling depression	Shallow basement	Thousands of meters to tens of kilometers	Hundreds of meters to 3—5 km	Control of secondary basins and structural belt sedimentary distribution, hydrocarbon accumulation and sealing combinations, and petroleum system
Tertiary fault controlling zone	Cap rock or upper part of shallow basement	6—12 km	Hundreds of meters	Control the formation and distribution of internal structural belts within the basin, and facilitate the migration of oil and gas between the source and reservoirs
Quaternary fault controlling block	Cap rock	3—6 km	40—100 m	Control the formation and distribution of local fault blocks, and regulate the redistribution of oil and gas
Quinary fault (low-order faults)	Intra-layer	< 3 km	< 40 m	Cause deformation and modification of local stratigraphy

and the EW strike faults were interpreted to be developed in different stages. For Type III, the fractal dimension value was distributed in 1.00 and 1.56 (Fig. 4e). The fractal dimension value of the nearly NW trending faults with medium-small extend length was significantly influenced by the large-scale faults. Generally, the medium-small scale faults exhibited fractal dimension value with relatively higher correlation in the same secondary tectonic area. For example, the Nan 4—2, Nan 4—3, Nan 4—5, and Nan 4—7 faults showed similar fractal dimension value with the Xin 120 and Xin 133 faults. Consequently, constrained by the secondary and tertiary activity, the fractal dimension value of the nearly NE-SW trending faults and the nearly E-W strike faults in the DXFZ was significantly different. Then the difference in the formation stages and the activity of the faults were distinguished between the two direction faults. Overall, the fractal dimension value of the NE-SW trending fault was higher than that of the E-W trending fault, revealing high fault activity intensity. The analyzed results of fractal dimension could be used to provide certain guidance and indication for the research on the fault activity.

4.3. Genetic mechanism analysis

Aiming at analyzing the complex genetic mechanism of different fault patterns, the stress-strain ellipse, developmental patterns, and rose flower diagram were adopt to verify the fault rationality and distinguish the stress mechanism of various faults (Fig. 5). Three different stress loading backgrounds were distinguished in the DXFZ, the pure shear, the single shear, and the diapir stress (Fig. 5a). Under the pure shear, the conjugate normal faults with high-angle were generated, exhibiting the symmetrical graben and horst structure. The stress-strain circle transformed from the initial circular shape to the horizontal stretching oval shape. Constrained by the single shear, the initial stress-strain shape has transformed from the circle to obliquely extending ellipse, performing as large-scale low-angle normal fault. The hanging wall showed rotational deformation and the footwall indicated the weak deformation. Due to the diapir stress, the top graben was generated. Then the ring-shaped and radial fault systems were formed at the top of the diapir core. Additionally, the oppositely inclined normal faults with same strike with the salt ridge were primarily formed on the top of the core. Combing the seismic profile interpretation with the theoretical pattern, the DXFZ has been interpreted to be experienced three different stress environments, indicating two significant tectonic backgrounds: extensive torsion and diapir upwelling. By means of structural trace and quantitative statistical tools, the active fault strikes of different levels in various periods were determined. Constrained by the

extension length and fault throw, five different fault levels were classified, the first-order fault (controlling the basin), the secondary fault (controlling the depression), the third-order fault (controlling the tectonic zone), the fourth-order fault (controlling the block), and low-order fault (Lu et al., 2019). Four different rose diagrams of different fault combinational types were distinguished, the active secondary faults, the active high-order faults (level 2—4), the active low-order faults, and all active faults in different periods. During the E_s^3 sedimentary period, the strikes of active secondary faults were primarily distributed in 80° and 100° (nearly EW trending). The strikes of the active high order faults were mainly concentrated in 30—60° and 80—100°. The orientations of the active subordinate faults were primarily distributed in 30—50°, 80—100°, and 120—140°. Additionally, three key strike distribution ranges of all active faults were distinguished, 30—60°, 80—100°, and 120—150° (Fig. 5b). Similarly, during the E_s^2 sedimentary period, the orientations of active secondary faults were mainly distributed in 80° and 100° (nearly EW trending). The strikes of the active high order faults were mainly concentrated in 30—50°, 80—100°, and 120—140°. The orientations of the active subordinate faults were primarily distributed in 30—60°, 80—100°, and 120—150°. Consequently, three significant strike distribution ranges of all active faults were distinguished, 30—60°, 80—100°, and 120—150° (Fig. 5b). Additionally, during the E_s^1 sedimentary period, the strikes of active secondary faults were primarily distributed in 80° and 100°. The orientations of the active high order faults were mainly concentrated in 30—60° and 80—100°, few in 120—140°. The strikes of the active subordinate faults were mainly distributed in 30—50°, 80—100°, and 120—150°, few in the 0—10° and 170—180°. Comprehensively, three key strike distribution ranges of all active faults were distinguished, 30—60°, 80—100°, and 120—150° (Fig. 5b).

Based on the above results, four different fault strikes were distinguished in the DXFZ, the nearly EW trending, the NE-SW strike, the NW-SE trending, and the nearly SN strike. Then the two significant stress environments were identified, the extensive torsion and diapir upwelling. In order to make a detail analysis on the mechanical formation mechanism, the multi-level derived structures were deeply summarized (Fig. 6). Generally, in a certain study area, the primary structure with a larger scale and a dominant role was called the main structure. The other primary structures generated by the initial stress field during the same forming period with the main structure was named as associated structures. A structure that was directly derived from a main structure was defined as a derived structure (Walsh and Watterson, 1991; Ferrill and Morris, 2001). During the NW-SE and NNE-SSW extensional tectonic movement, three different orders were divided into the

(a)

(b)
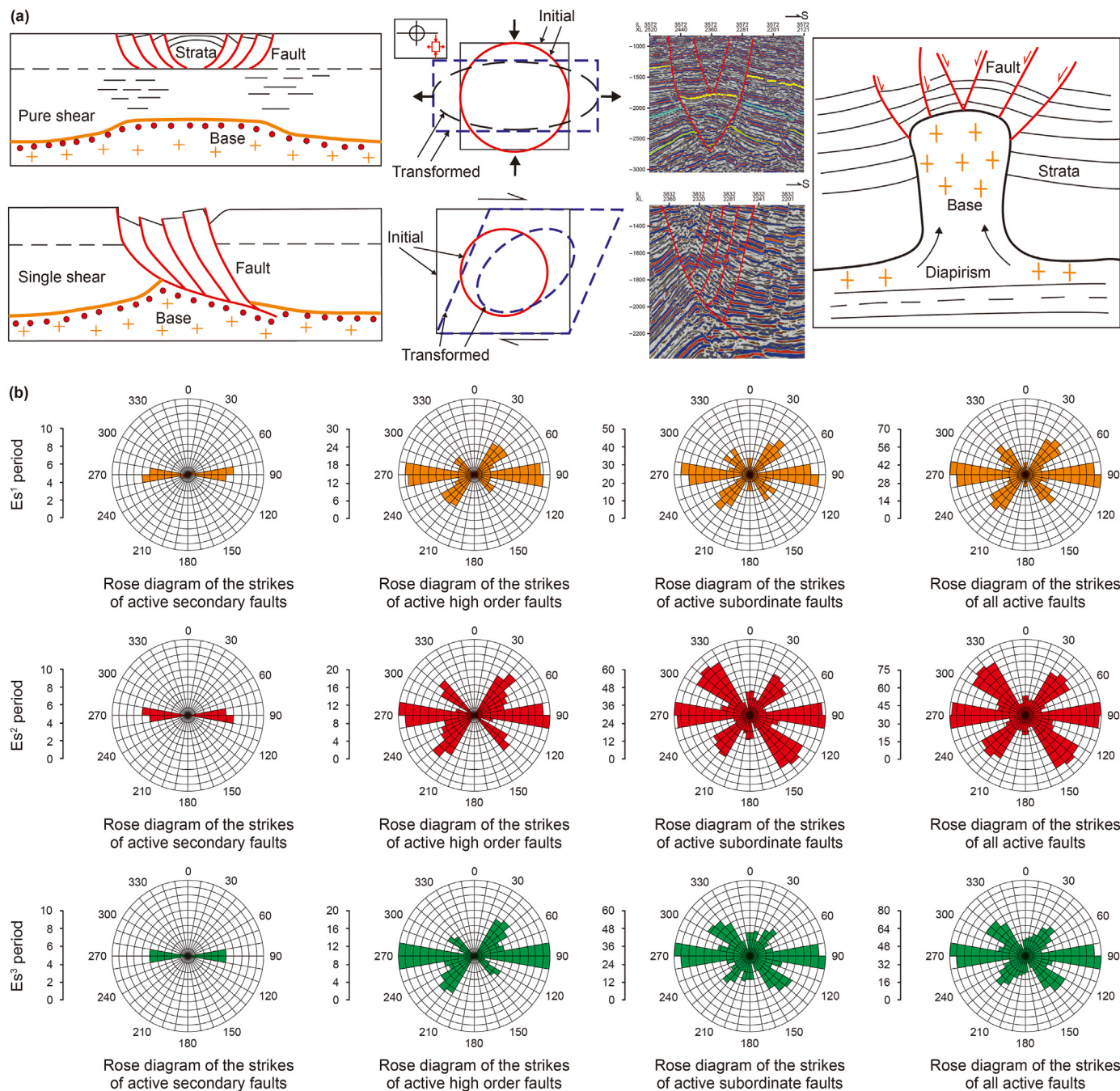
Fig. 5. (a) Genesis mechanism of faults under pure shear stress and single shear stress and schematic diagram of the corresponding seismic section; (b) rose diagrams of the strikes of active faults with different levels during the E_s^3, E_s^2, and E_s^1 periods, where the yellow color is for E_s^1 period, the red color shows the E_s^2 period, and the green color refers to the E_s^3 period.

structural traces formed within a certain range, the first order (nearly EW-trending extensional fault), the second order (SEE-NWW strike extensional fault), and the third order (NW-SE trending normal fault). Basically, the secondary structure derived from the fault could be conducted to determine the relative movement direction of fault wall, where the $\sigma_3 < 0$, $\sigma_1 > 0$, and the magnitude of σ_3 was larger than σ_1, the developmental pattern belonged to the A_1-A_2-A_3 or A_4 (Fig. 6). The conjugate normal fault and symmetrical graben were generated, and the low angle normal faults were also formed. Illustratively, constrained by the local compressive stress, the σ_1, σ_2, and σ_3 were all larger than 0, the

developmental pattern of the fault belonged to the B_1−B_2 or C_2−C_3. Then some secondary faults with small scale and NE-SW or NW-SE trending were generated (Fig. 1c). These mechanical patterns could be used to explain the faults with abnormal throw during the background of a large extensional stress.

4.4. Typical fault patterns and characteristics in the DXFZ

Constrained by the complex stress environments, typical fault patterns and characteristics were summarized in the DXFZ. Primarily three significant stress backgrounds were identified, the
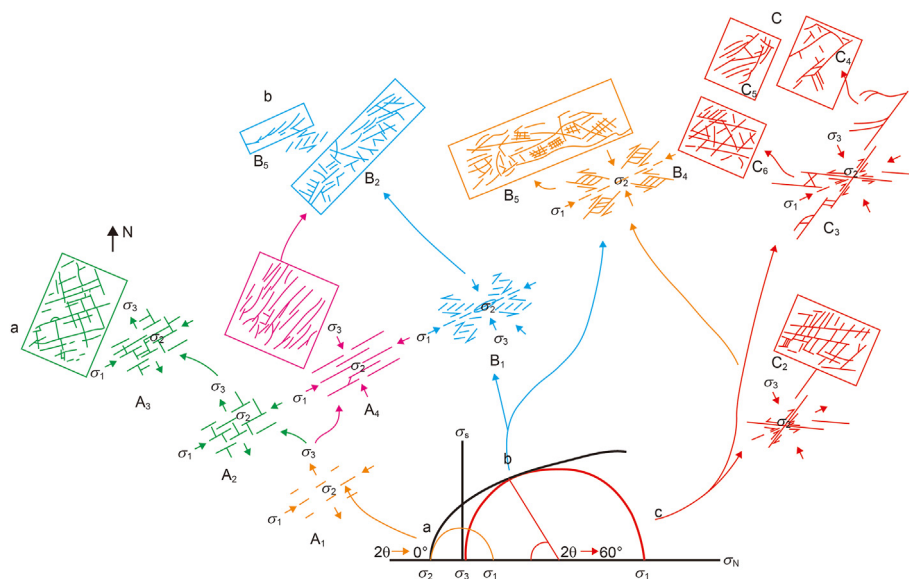
Fig. 6. The mechanical formation mechanism of DXFZ under the combined stressed of extension and diapir.

extensional, tensile torsional, and diapir upwelling stress environment (Fig. 7). Combining the developmental characteristics of horizon with the profile, seven different style classifications were distinguished: the linear, the fusiform, the wedge-shaped, the parallel, the "Y" shape, the step fault, and the graben and horst (Fig. 7). The linear fault was mostly small scale and used to connect two faults, paralleling to the faults of the same type. Generally, the fusiform fault was developed independently, showing a slight arc on the plane. The wedge-shaped fault was mostly developed at the ends of faults. Constrained by the same stress environment, the faults with the same nature, equal scale, and equal spacing performed parallel with each other. The "Y" shape fault was composed of a main fault and the corresponding low-order fault on the hanging wall, showing a "Y" shape in section. Additionally, the step fault was composed of several normal fault with the same occurrence, and the hanging wall broke in the same direction in turn. The graben and horst were composed of two faults with roughly parallel strikes, opposite inclinations, and the same nature. The graben shared a downthrown wall and the horst shared an upthrown wall. These visible characteristics indicated a typical extensional stress environment in the DXFZ.

Based on the developmental characteristics of horizon and profile, seven significant style classifications were identified, the wave shape, the linear shape, the arc shape, the echelon shape, the broom-like, the oblique fault, and the flower-like fault (Fig. 7). Interpretatively, the wave shape fault was long-extended, appearing on the secondary and tertiary faults. The arc shape fault was prone to develop in broom faults in combination. Additionally, the echelon shape faults were composed of several normal faults, reverse faults, or slip faults of the same nature with equal scale and spacing on the plane. The broom-like faults were composed of several arc-shaped faults, converging to one end and spreading out to the other end (Fig. 7). The concave side wall of the shear broom-shaped fault moved in the convergent direction relative to the convex side wall. For the oblique fault, a fault did not intersect perpendicularly and terminated on the top of another fault. The limiting fault shoed a shear property, and the confined fault indicated a normal fault. The flower-like fault was observed in the study area, it usually performed as a combination of upwardly bifurcated

and scattered faults in the shallow part. Basically, a flower-like structure formed by the tension-shearing was named as negative flower-like structure. The observed phenomenon revealed that the DXFZ has experienced the tensile torsional stress.

By integrating the statistical characteristics of horizon and profile in the research area, four key style classifications were distinguished, the arc shape, the ring-shaped and radial fault, the salt ridge top graben, and the turtle structure. The ring-shaped fault was composed of several arc or semi-arc faults arranged in concentric circles around a center. The radial fault was formed by several faults radiating from a center. Generally, the graben was a ring-shaped and radial fault system at the top of the diapir core. In the overlying strata of the core top, the formed faults were consistent with the strike of the salt ridge and inclined opposite to each other. The turtle structure was characterized with two or more salt diapir cores growing roughly synchronously. The salt supra-layer between the salt diapir cores could develop into a concave-convex tortoise-shaped anticline structure. Comprehensively, these visible style classifications both in the horizon and profile indicated three significant stress backgrounds, the extensional stress, the tensile torsional stress, and the diapir upwelling stress. Especially, the tensile-torsional stress and diapir upwell stress were the two key tectonic stress environments for generating the FAZ in the DXFZ.

5. Discussion

In order to comprehensively analyze the formation mechanism of fault accommodation zones under combined stress in graben basin, methods of tectonic physical simulation experiment and finite element numerical simulation were conducted in this manuscript. Through the results and comparison in different sedimentary periods, the developmental characteristics of FAZ were obtained. Then the rupture characteristics in different sedimentary periods were quantitatively calculated. Consequently, the tectonic evolution model of DXFZ was summarized, and the research results could provide a novel way to analyze the formation mechanisms of accommodation zones.
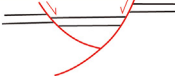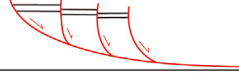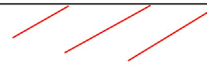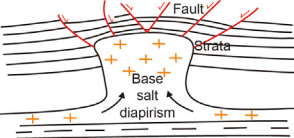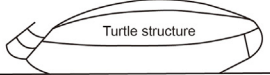
Stress Background	Style classification			Typical examples	Feature description
Extensional environment	Horizon	Single	Linear		Mostly small faults connecting two faults, often parallel to the strike of faults of the same type.
			Fusiform		A small fault developed independently, compared with the straight type, the plane shape shows a slight arc.
			Wedge-shaped		Mostly develops at the ends of faults.
		Combi-nation	Parallel		The faults in the same combination are of the same nature, equal scale, and equal spacing. Parallel faults are generally formed in the extensional stress.
	Profile	Combination	"Y" shape		The fault is composed of the main fault and the corresponding low-order fault on the hanging wall, performing a "Y" shape in section
			Stepped fault		It consists of several normal faults with basically the same occurrence, and the hanging wall of each fault breaks in the same direction in turn.
			Graben and horst		Grabens and horsts are composed of two faults with roughly parallel strikes, opposite inclinations and the same nature. Grabens share a downthrown wall and horsts share an upthrown wall.
Tensile torsional stress	Horizon	Single	Wave shape		Most of them are long-extended faults, often appearing on secondary and tertiary faults.
			Linear shape		Mostly small faults connecting two faults, often parallel to the strike of faults of the same type.
			Arc shape		During the tensile-torsional stress, it often occurs in broom faults in combination.
		Combination	Echelon shape		The faults are composed of several normal faults, reverse faults or slip faults of the same nature with equal scale and spacing in an echelon pattern on the plane.
			Broom-like		It is composed of several arc-shaped faults, converging to one end and spreading out to the other end. The concave side wall of the shear broom-shaped fault moves in the convergent direction relative to the convex side wall.
			Oblique fault		A fault does not intersect perpendicularly and terminates on top of another fault. The limiting fault shows a shear property, and the confined fault indicates a normal fault.
	Profile		Flower-like		In the shallow part, faults usually performs as a combination of upwardly bifurcated and scattered faults. It is a flower-like in section, and the flower-like structure formed by the nature of tension-shearing was named as negative flower-like structure.
Diapir upwelling	Horizon	Single	Arc shape		During the diapiring action, influenced by the uplift, the arc or semi-arc faults primarily develops in ring-shaped and radial faults.
		Combination	Ring-shaped and radial fault		A ring-shaped fault is composed of several arc or semi-arc faults arranged in concentric circles around a center. The radial fault is formed by several faults radiating from a center.
	Profile		Salt ridge top graben	Fault / Strata / Base salt diapirism	The graben is usually a ring-shaped and radial fault system at the top of the diapir core. In the overlying strata of the core top, the formed faults are consistent with the strike of the salt ridge and inclined opposite to each other.
			Turtle structure	Turtle structure	Two or more salt diapir cores grow roughly synchronously. The salt supralayer between the salt diapir cores can develop into a concave-convex tortoise-shaped anticline structure.

Fig. 7. The typical structural styles of different stress backgrounds in the study area.

5.1. Tectonic physical simulation experiment of the fault activity in the Dongxin fault zone

In order to realistically restore the complex tectonic stress environment and evolution process, three significant periods were simulated during the tectonic physical simulation experiment. The fault prototypes of Ying 8, Ying 1, Ying 31, and Xin 120 formed during the sedimentary period of $E_k-E_s^4$ were preset. During the first period, aiming to simulate the dextral strike-slip action, the stable and continuous EW-strike extensional stress was loaded on the north of the eastern border and the south of the western border. The NNE-SSW-strike extensional stress was loaded on the north

and south borders to simulate the NNE-SSW extension. During the second period, the dextral strike-slip action was strengthened, and the NNE-SSW extensional stress was relatively weakened. Then the NE-strike extensional stress was gradually enhanced. During the third period, the NE-strike extensional stress was further strengthened. Simultaneously, the silicone was injected into the rectangular and oval vacuum bags to simulate the diapir upwelling in the plastic layer.

During the extensive torsion stress (I period), influenced by the Ying 8 and Xin 120 faults, the Xin 23 and Xin 1 faults were developed in the Xinzhen tectonic zone in the E_s^4 (5.6 min) sedimentary period (Fig. 8a). Constrained by the NNE-SSW-strike extensional stress, the EW-strike graben faults and Ying 1 fault were developed in the upper E_s^3 (8.9–9.5 min) sedimentary period (Fig. 8b–d). Simultaneously, the Xin 109 fault accommodation zone (FAZ) and Xin 120 FAZ were initially formed. With the increase of dextral strike-slip and extension (second period), the major faults in the DXFZ developed and formed. Constrained by the continuous extensive torsion stress, the fault shape performed as the wave gradually during the upper-middle E_s^3 (14.7–16.2 min) sedimentary period (Fig. 8e). The Xin 109 FAZ and Xin 120 FAZ were furtherly developed, and the FAZ between.

Ying 1 fault and Ying 31 fault were developed. Influenced by the

uneven stress in the plastic layer (third period), the study area occurred localized upper arch. During the E_s^2 (17.3 min) sedimentary period, the radial faults of the DXFZ were obviously developed. Then the low-order faults between the Xin 1 fault and Xin 120 fault were further complicated in the Xinzhen tectonic zone (Fig. 8f). Simultaneously, the Xin 15 FAZ and Xin 109 FAZ were furtherly developed. With the increase of the NE-strike extensional stress and dextral strike-slip stress, the NNE-SSW strike faults were derived in the southwest of the DXFZ. The broom-like faults were derived in the Ying 1 fault. The Ying 26 FAZ between the tail of the Ying 1 fault and the head of the Ying 31 fault were developed and formed (Fig. 8g). Then the DXFZ was developed and formed during the E_s^1 (17.3 min) sedimentary period (18.9 min). Influenced by the weaken of the tectonic activity, the activity of faults in E_d sedimentary period (19.6 min) was weakened, then the DXFZ was developed and shaped (Fig. 8h). In order to regulate the uneven stress and deformation, the FAZ among the major faults were finally developed and formed in the DXFZ.

5.2. Numerical simulation of the stress field during the E_s^3 sedimentary period

Constrained by the developmental characteristics of active
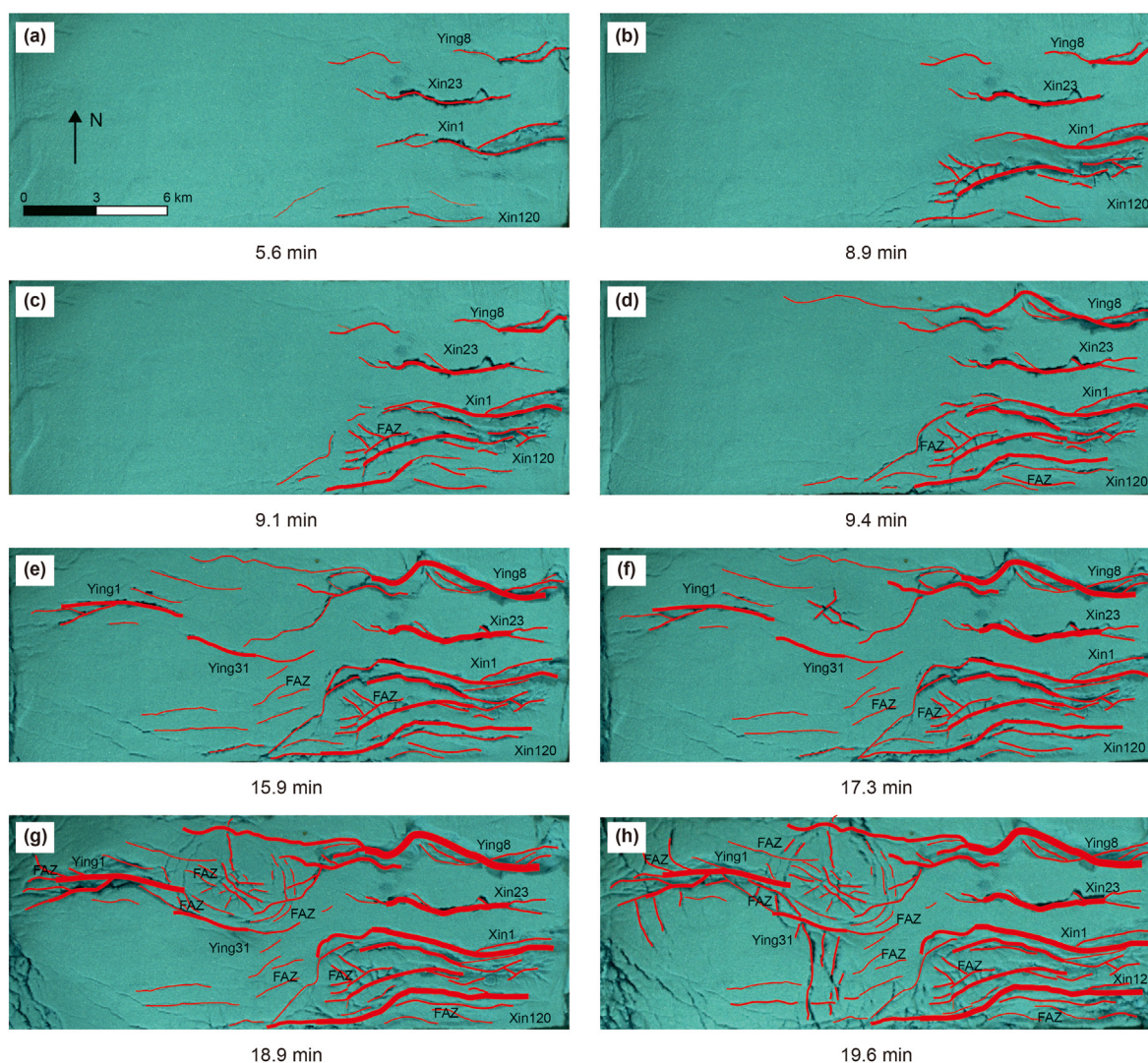

Fig. 8. The experiment results of tectonic physical simulation in the Dongxin fault zone.

faults during the E_s^3 sedimentary period, a geological model with a size of ~9 km × 25 km was established to simulate the developmental process of the DXFZ based on the finite element software (ANSYS 15.0). During the modeling process, the study area boundary, the active faults, and the topographic relief were established according to the actual situation (Fig. 9a). Similar to the tectonic physical simulation experiment, the fault prototypes of Ying 8, Ying 1, Ying 31, and Xin 120 formed during the sedimentary period of E_k—E_s^4 were preset. The total thickness of the E_s^{3+4} Formation was set to 500 m. Constrained by the triaxial rock mechanical testing, the rock mechanical parameters of the strata were obtained. Empirically, due to the complexity of fault structure and limitation of the tested means, the rock mechanical parameters of faults were difficult to determine by the logging interpretation and rock mechanical experiments. Basically, the modulus of faults was lower and the Poisson's ration was higher than those of the strata (Liu et al., 2017; Ren et al., 2019; Liu et al., 2022). Based on the previous experience, the various rock mechanical parameters were assigned to the strata and faults (Table 2). Constrained by the meshing method of Solid 45 element, the geomechanical model of the DXFZ was established by the finite element software. The Solid 45 element was a kind of finite element body suitable for the stress field simulation in the layered sedimentary rocks. And the geological model could be meshed through the free grid division and discretized as numerous nodes and elements. The listed numbers of the nodes and elements in different sedimentary period was shown in Table 3.

Due to the short-term and instantaneous process in the numerical simulation, a method of equivalent stress field was adopted to exhibit a long-term tectonic movement process (Kimura et al., 2003; Mohammadnejad and Andrade, 2016; Liu et al., 2018). The formation extension was the total amount of basement extension in

Table 2
The rock mechanical parameters in the paleo stress field of the Dongxin fault zone in the numerical simulation.

	Young's modulus, GPa	Poisson's ratio	Rock density, kg/m^3
Strata	4.5	0.18	2580
Fault	3.5	0.24	2400
Frame	4.2	0.22	2450

Table 3
Numbers of nodes and elements of the finite element models during the simulation.

Period	E_s^3 period	E_s^2 period	E_s^1 period
Element number	758019	946652	652863
Node number	148073	180428	130328

the profile, the horizontal expansion index was defined as basement extension per unit length and the vertical was the extension ratio amount overtime (Liu et al., 2022). Based on the formation expansion index, the corresponding magnitudes of the tectonic stress during the various periods were determined. Referenced by the strike of the active faults during a certain period, the direction of the paleo stress could be obtained (Fig. 5b). Additionally, the vertical stress was automatically generated by the numerical simulation software. Through constantly modifying the loading methods, the simulated results were primarily applied to match the fault activity and structural features. Consequently, a NE-SW (20—200°) tensile stress (17 MPa), a NW-SE (110—290°) tensile stress (48 MPa), and a NE-SW dextral shear stress (25 MPa) were applied along the boundary of the strata framework (Fig. 9b). The loaded stress conditions were similar to the Dongying Sag during the period (Xian et al., 2018; Lu et al., 2019; Wang et al., 2020),
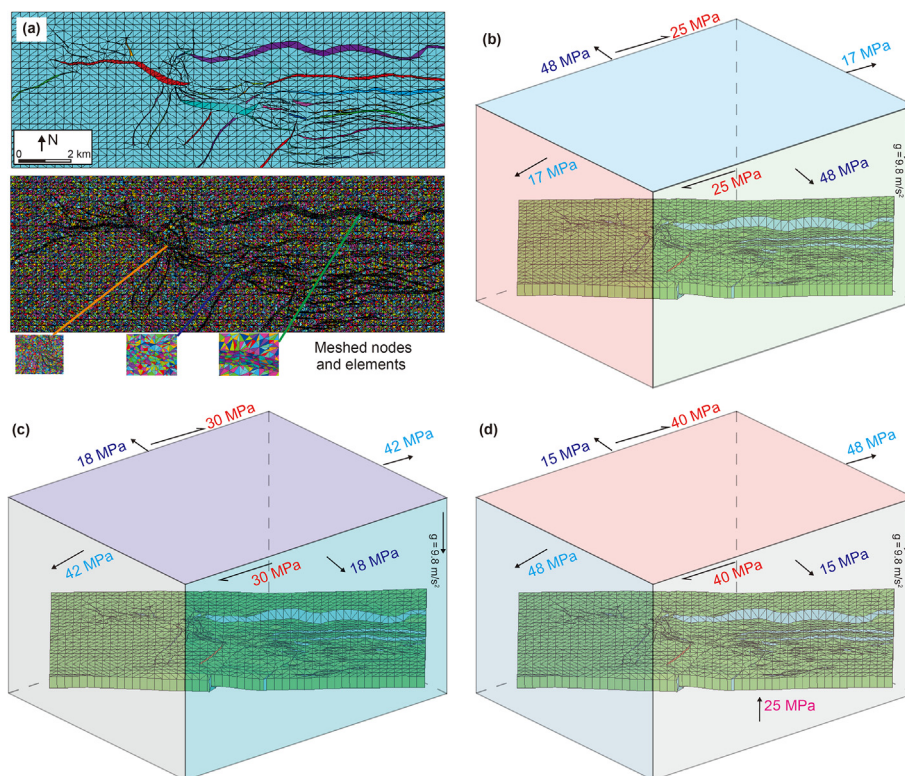
Fig. 9. The modeling and loading conditions of finite element geological model. (a) is the geological mechanical strata and fault model; (b, c, d) show the boundary and loading conditions during the E_s^3 period, the E_s^2 period, and the E_s^1 period, respectively.

showing consistent with the stress loading methods of the tectonic physical simulation experiment. The loaded stress magnitude was shown in Fig. 9b, and the bottom surface was set to a displacement constraint along the z direction to meet the finite element simulation. Then the paleo stress field during the E_s^3 period was simulated (Fig. 10). Illustratively, the negative value in the software indicated the compressive stress, and the positive value in the software showed the extensional stress. This situation was the opposite of the traditional geological statement, however, it did not make any influence on analyzing the developmental characteristics of the in-situ stress. Constrained by extensional and the dextral shear action of the Tan-Lu fault zone, the Bohai Bay Basin was characterized with the compound stress of NE-SW strike and NW-SE strike stress, and the dextral stress (Zhang et al., 2010; Lu et al., 2019).

During the E_s^3 sedimentary period, the simulated results showed that the horizontal minimum principal stress was tensile (positive value in the software; Fig. 10a). The high values were concentrated in the nearly EW-strike faults (Ying 1, Ying 31, Ying 8, and Xin 120). The local stress near the Ying 8 fault was compressive (negative value in the software). The junction area of two large-scale faults were characterized with relatively high tensile stress. The high values of the intermediate principal stress were highly related with the Ying 8 fault, Ying 31 fault, and Ying 1 fault (Fig. 10b). Influenced by the EW strike fault action, the junction area of the horizontal maximum principal stress indicated a high tensile value (yellow-red area, Fig. 10c). In some area, such as the Ying 66 FAZ and Ying 26

FAZ, the strata were characterized with a large compressive stress (blue area). The stress intensity (σ_1-σ_3) revealed high values in the nearly EW-strike faults and the junction area of two large-scale faults (Fig. 10d). Especially, the Ying 66 FAZ, Ying 26 FAZ, Ying 8 FAZ, and Xin 120 FAZ were characterized with relatively high stress intensity value, indicating the area prone to rupture. The horizontal minimum principal stress could be applied to indicate the fault activity (Liu et al., 2018, 2022). And the stress intensity could be applied to analyze the fracturing area (Ren et al., 2019). The minimum principal stress of the EW-strike fault with large scale was high, while that on the NW-SE strike faults was low, indicating good agreement with the fault activity characteristics (Fig. 4a and b). Additionally, the stress intensity indicated similar distribution characteristics with the minimum principal stress. This phenomenon revealed the high consistency with the fault activity characteristics (Fig. 10d). The planar shear stress (τ_{xy}) in the DXFZ during the E_s^3 sedimentary period was primary positive value, few with negative value (Fig. 10e). The study area indicated a tectonic environment of right-lateral and left-lateral slip action. The stress intensity strain near the nearly EW-strike fault, the junction area of two similar large-scale faults, and the FAZ was larger than that on the NW-SE strike faults (Fig. 10f). It showed good agreement with the calculated results with the fractal dimension results (Fig. 4c—e). Constrained by the differences in the stress, strain, and fault activity in the various faults, the dynamic mechanism of the DXFZ development primarily included the convergent FAZ, overlap FAZ, approach FAZ, and parallel FAZ. Based on the Coulomb-Mohr
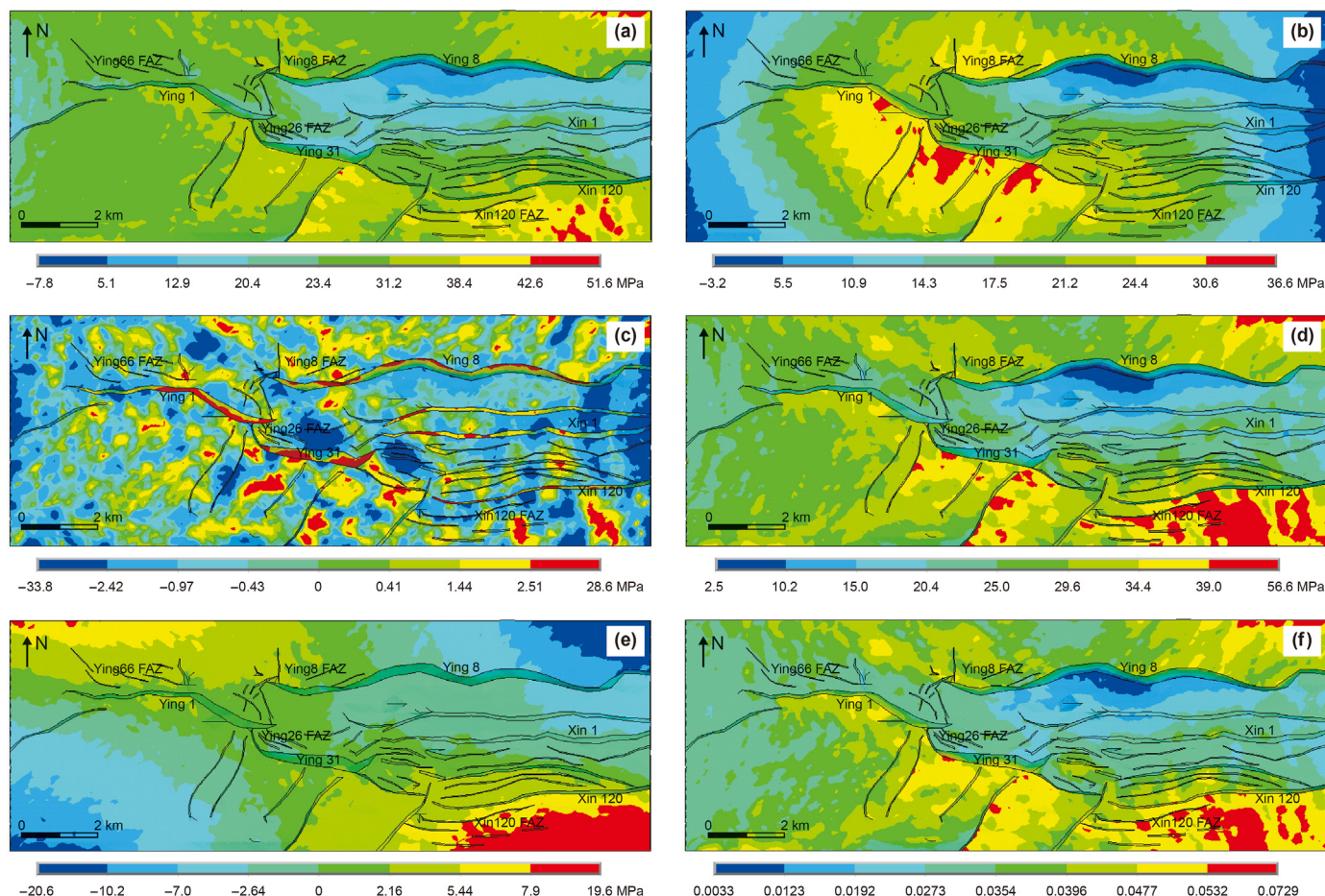

Fig. 10. The paleo stress simulation results during the E_s^3 period in the study area. (a) is the minimum principal stress (σ_3); (b) shows the middle principal stress (σ_2); (c) refers to the maximum principal stress (σ_1); (d) is the stress intensity (σ_1-σ_3); (e) shows the plane XY shear stress; (f) indicates the elastic strain intensity.

rupture criterion, the NW-strike and NNE-strike faults were prone to be generated, showing high consistency with the strikes of active faults during the period.

5.3. Numerical simulation of the stress field during the E_s^2 sedimentary period

Constrained by the distribution characteristics of the active faults during the E_s^2 sedimentary period, a geological model consist of the strata and faults were established to simulate the midterm development of the Dongxin fault zone. Based on the top structural form of the E_s^2 Formation, combined with the seismic interpretation, the active faults, and study area boundary, the comprehensive geological model were established. The thickness of the E_s^{4+3+2} Formation was set to 800 m in the finite element numerical simulation software. The Young' modulus, Poisson's ratio, and density of the faults and strata were shown in Table 2, and the meshed elements and nodes were shown in Table 3. Similar to the tectonic physical simulation experiment, based on the trend of the active faults during the E_s^2 sedimentary period, a NNE-SSW (20−200°) tensile stress (42 MPa), a NW-SE (110−290°) tensile stress (18 MPa), and a NE-SW dextral shear stress (30 MPa) were applied along the boundary of the study area (Fig. 9c). The vertical stress was automatically generated by the numerical simulation software. Similarly, through constantly modifying the loading methods, the simulated results were primarily applied to match the fault activity and structural features. The loaded stress magnitude was shown in Fig. 9c, and the bottom surface was set to a displacement constraint along the z direction to meet the finite element simulation. Consequently, the paleo stress field during the E_s^2 sedimentary period was simulated.

The simulated results indicated that the horizontal minimum principal stress was tensile during the E_s^2 sedimentary period (Fig. 11a). Similarly, the high values were concentrated in the nearly EW-strike faults (Ying 1, Ying 31, Ying 8, and Xin 120), and the high value area has expanded than that during the E_s^3 sedimentary period. The local stress near the Ying 8 fault was compressive. Additionally, the relatively high tensile stress was distributed in the junction area of two large-scale faults, especially in the Ying 66 FAZ, Ying 8 FAZ, Ying 26 FAZ, and Xin 120 FAZ. The high values of the intermediate principal stress were primarily distributed along the nearly EW-strike fault and near the junction area of two similar faults (Fig. 11b). Constrained by the EW-trending faults, the junction area of the horizontal maximum principal stress was characterized with a high tensile value (yellow-red area, Ying 26 FAZ, Fig. 11c). Along the EW-strike faults, the maximum principal stress indicated a high tensile value. The low tensile value of the maximum principal stress was distributed in the NE-SW trending faults (blue area). The stress intensity (σ_1-σ_3) indicated high values (29.9−56.5 MPa) in the Ying 1 fault, Ying 31 fault, Ying 8 FAZ, Xin 120 fault, and Xin 120 FAZ area (Fig. 11d). The stress intensity strain near the nearly EW-strike fault (Ying 1, Ying 31, Xin 120), the junction area of two similar large-scale faults (NE-SW trending faults), and the FAZ (Ying 66, Ying 26, Ying 8, and Xin 120) was larger than that on the NW-SE strike faults (Fig. 11f), indicating basic agreement with the calculated results with the fault activity and fractal dimension results. During the E_s^2 sedimentary period, the stress, strain, and fault activity were also different in the various faults, reflecting the inherited characteristics of the convergent FAZ, overlap FAZ, approach FAZ, and parallel FAZ in the DXFZ during the E_s^3 sedimentary period.

The minimum principal stress of the EW-strike fault with large scale was significantly high, mainly produced symmetrical graben-horst faults. Similarly, the planar shear stress (τ_{xy}) in the DXFZ during the E_s^2 sedimentary period indicated a tectonic environment

of left-lateral and right-lateral slip action (Fig. 11e). Then the NE-SW trending faults were prone to be generated. The analyzed results exhibited a good consistency with the seismic interpretation (Figs. 5a and 7). Constrained by the Coulomb-Mohr rupture criterion, the simulated results showed that the northern section of the study area exhibited a strong extensional-torsional stress and primarily generated south-dipping faults and converge FAZ. The middle section indicated a weak extensional-torsional stress and mainly produced counter-dipping normal faults, overlap FAZ, and approach FAZ. However, the southern section of the study area indicated strong tensile-lateral stress and primarily generated north-dipping faults, SE-dipping faults, and parallel FAZ, showing good agreement with the simulated results of tectonic physical simulation experiment (Fig. 8).

5.4. Numerical simulation of the stress field during the E_s^1 sedimentary period

Constrained by the distribution characteristics of the active faults, a geological model was established to simulate the paleo stress field of the DXFZ during the E_s^1 sedimentary period. The thickness of the Shahejie Formation was set to 1000 m. The built model contained the undulation features of the target formation. The mechanical parameters (Young's modulus, Poisson's ratio, and density) of the fault and strata were listed in Table 2. The meshed numbers of the element and node were shown in Table 3. Similarly, through analyzing the strike of the active fault during the E_s^1 sedimentary period, the combined stress of dextral strike-slip and diapir upwelling was determined. Consequently, a NE-SW (20−200°) tensile stress (48 MPa), a NW-SE (110−290°) tensile stress (15 MPa), and a NE-SW dextral shear stress (40 MPa) were applied along the boundary of the strata framework (Fig. 9d). Additionally, a diapir stress (25 MPa) was conducted on the bottom surface to simulate the diapir upwelling action. Similarly, through constantly modifying the loading methods, the simulated results were primarily applied to match the fault activity and structural features. The vertical displacement constraint was set to the bottom surface to meet the finite element simulation. Consequently, the paleo stress field during the E_s^1 sedimentary period was simulated.

The simulated results indicated that horizontal minimum principal stress during the E_s^1 sedimentary period was tensile (Fig. 12a). The minimum principal stress decreased from north to middle area, and then increased to the south. The high values were primarily distributed in the large-scale faults (EW-strike and NE-SW trending), junction area of two similar faults, and several FAZ (Ying 66, Ying 8, Ying 26, and Xin 120). Similarly, the high value area furtherly expanded than that during the E_s^2 sedimentary period. The high values of the intermediate principal stress were primarily distributed along the nearly EW-strike fault, Ying 8 FAZ, Xin 120 FAZ, and near the junction area of two similar faults (Fig. 12b). Influenced by the EW-trending and NE-SW strike faults, the horizontal maximum principal stress indicated high values in the junction area of Ying 8 and Xin 1 fault, Ying 1 fault, Ying 31 fault, Ying 26 FAZ, and Ying 8 FAZ (Fig. 12c). The low tensile value of the maximum principal stress was distributed in the Xin 120 FAZ (blue area). The stress intensity (σ_1-σ_3) indicated high values (29.4−45.6 MPa) in the Ying 1 fault, Ying 31 fault, Ying 8 fault, Ying 8 FAZ, Xin 120 fault, and Xin 120 FAZ area (Fig. 12d). The stress intensity strain near the nearly EW-strike fault (Ying 1, Ying 31, Xin 120), the junction area of two similar large-scale faults (NE-SW trending faults), and the FAZ (Ying 66, Ying 26, Ying 8, and Xin 120) was larger than that on the EW-trending faults with medium scale (Fig. 12f), indicating basic agreement with the calculated results with the fault activity and fractal dimension results. During the E_s^1 sedimentary period, the stress, strain, and fault activity also
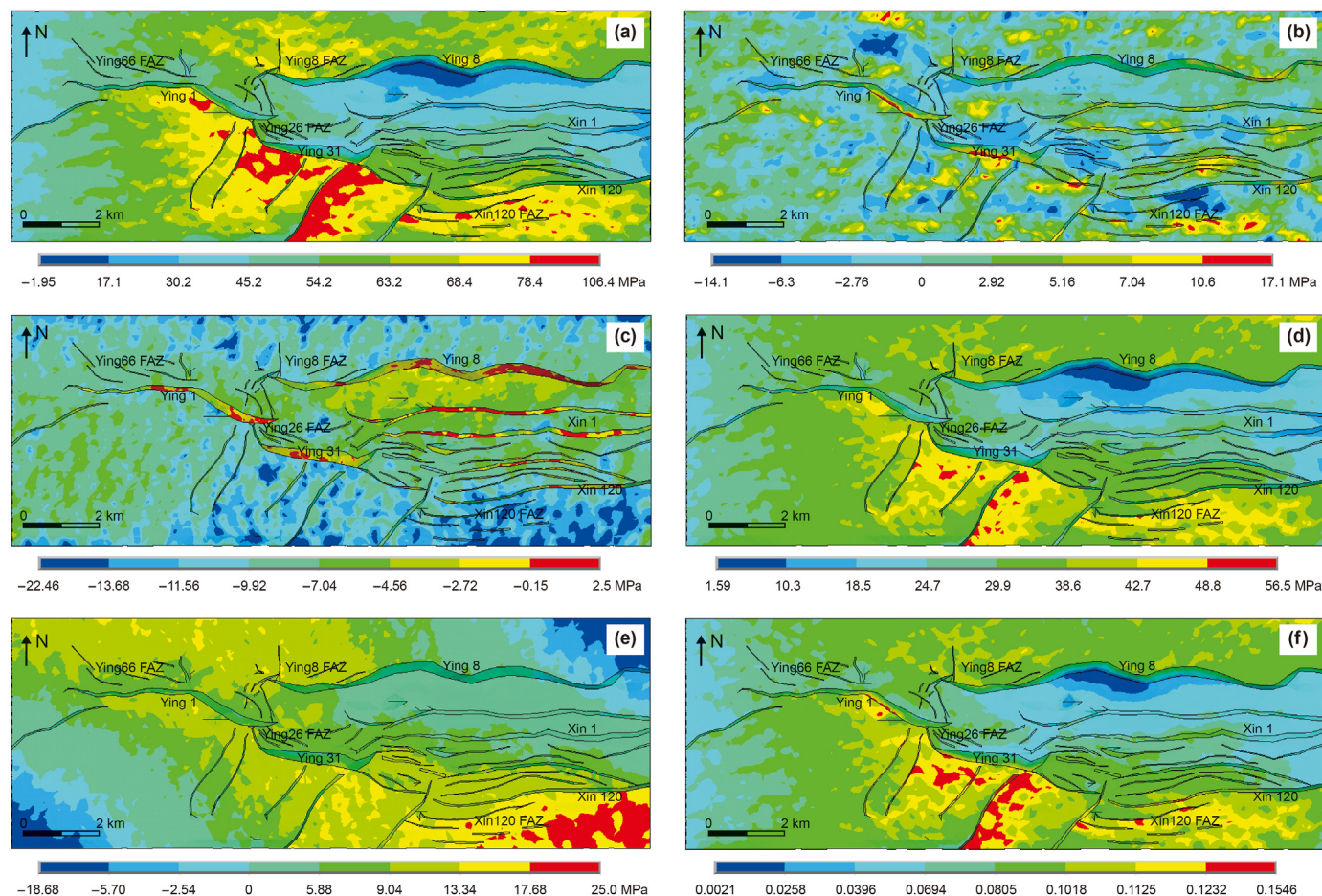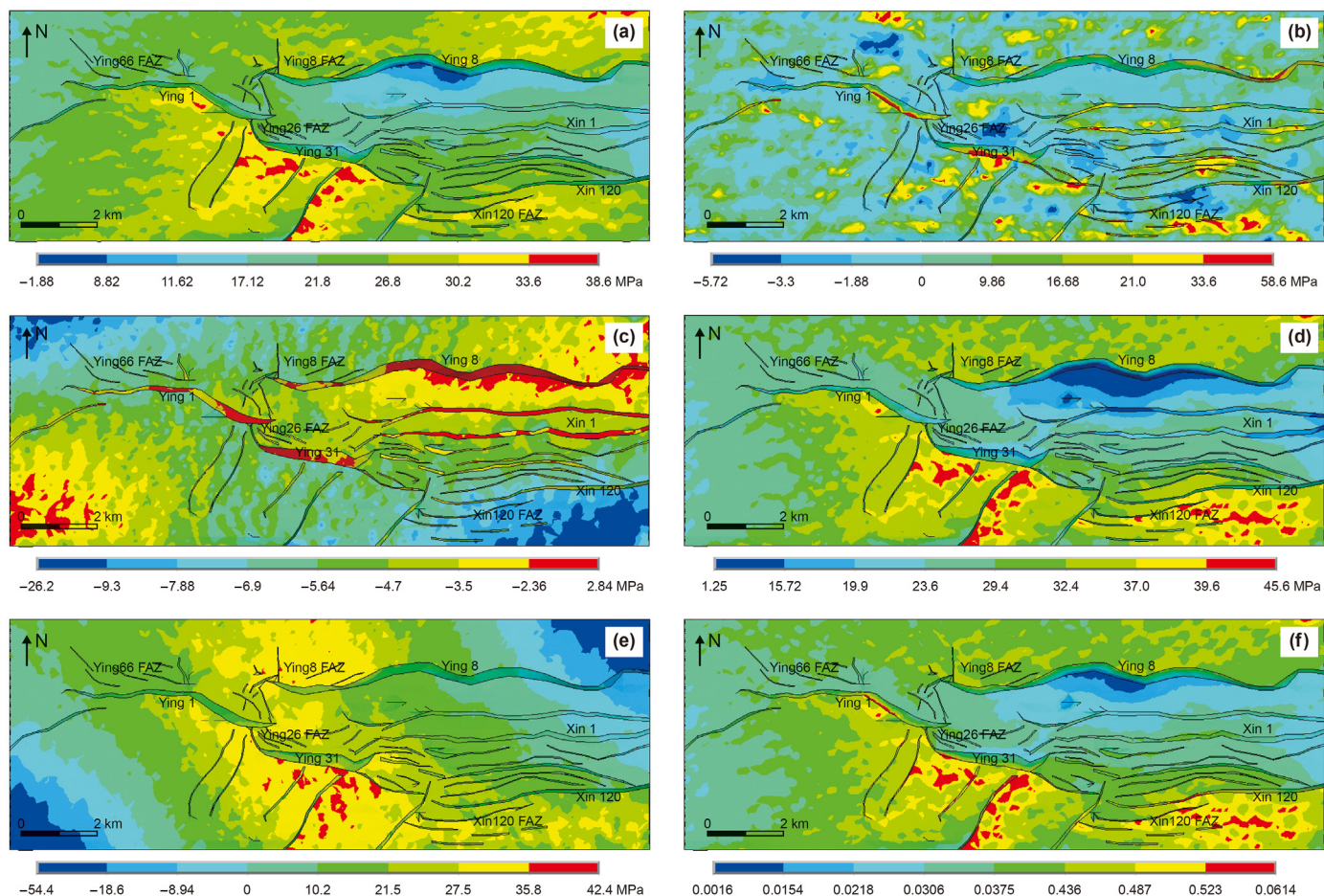
Fig. 11. The paleo stress simulation results during the E_s^2 period in the study area. (a) is the minimum principal stress (σ_3); (b) shows the middle principal stress (σ_2); (c) refers to the maximum principal stress (σ_1); (d) is the stress intensity (σ_1-σ_3); (e) shows the plane XY shear stress; (f) indicates the elastic strain intensity.

exhibited the difference in the various faults, reflecting the inherited characteristics of the convergent FAZ, overlap FAZ, approach FAZ, and parallel FAZ in the DXFZ during the E_s^2 sedimentary period. The minimum principal stress of the EW-strike and NE-SW trending fault with large scale was significantly high, mainly produced symmetrical graben-horst faults and NW-SE strike slip faults. Similarly, due to the strengthening of dextral strike-slip, the planar shear stress (τ_{xy}) in the DXFZ during the E_s^1 sedimentary period indicated a tectonic environment of both left and right lateral slip action (Fig. 12e). Then the NW-SE- and NS-trending faults were prone to be formed. According to the Coulomb-Mohr rupture criterion, the simulated results showed that the northern section of the study area exhibited a strong extensional-torsional stress and primarily continuously developed south-dipping faults and converge FAZ. However, the southern section of the study area indicated strong tensile-lateral stress and primarily generated north-dipping faults, SE-dipping faults, and parallel FAZ, showing good agreement with the simulated results of tectonic physical simulation experiment (Fig. 8). Additionally, influenced by the diapir upwelling, the junction area of Ying 8 and Ying 1 fault indicated a strong upwelling action, primarily developing radioactive faults and convergent FAZ. The junction area of the Ying 8 and Xin 120 faults exhibited extension and upwelling stress, mainly producing NW-SE trending faults. The simulated results also show good consistency with the strike of the active faults during the period.

5.5. Rapture characteristics during different periods

Constrained by the paleo stress simulation results, combined with the Coulomb-Mohr rupture criterion, the fracture volume density and fracture aperture were calculated in the numerical simulation software during three different periods. The simulated results indicated that the high fracture volume density during the E_s^3 sedimentary period was primarily distributed in the southern section of the study area (Fig. 13a). Especially, the developed fracture area was mainly along the large-scale faults (EW- and NE-SW-trending) and junction area of two similar scale faults (0.629—1.814 m^2/m^3). Additionally, The Ying 8 FAZ, and Xin 120 FAZ area were prone to be raptured and easily developed fault accommodation zone, regulating the strain energy and deformation of Ying 8 fault and Xin 120 fault. Constrained by the energy conservation law, where the rupture density was high, where the rupture aperture was small (Liu et al., 2017; Ren et al., 2019). The fracture aperture during the E_s^3 sedimentary period showed the opposite distribution trend with the fracture volume density (Fig. 13b). Illustratively, the up wall of Ying 8 fault area and the middle section of the study area showed large fracture aperture, exhibiting relatively high consistency with the seismic interpretation (Fig. 3a). Similarly, the developed fracture area during the E_s^2 sedimentary period was mainly concentrated in the nearly EW-trending faults (large scale), NE-SW strike faults (large scale), and the junction area between the two large scale faults (southern section area, 2.48—6.63 m^2/m^3) (Fig. 13c). Emphatically, the Ying 8 FAZ, Xin 120

Fig. 12. The paleo stress simulation results during the E_s^1 period in the study area. (a) is the minimum principal stress (σ_3); (b) shows the middle principal stress (σ_2); (c) refers to the maximum principal stress (σ_1); (d) is the stress intensity (σ_1-σ_3); (e) shows the plane XY shear stress; (f) indicates the elastic strain intensity.

FAZ, Ying 26 FAZ, and Ying 66 FAZ exhibited relatively high fracture volume density, indicating strong ability to rupture and develop faults. Then the energy and deformation between two main faults (such as Ying 1 and Ying 31 fault) could be regulated. And the corresponding fault accommodation zone was produced, such as convergent FAZ, overlap FAZ, approach FAZ, and parallel FAZ (Figs. 1a and 13c). The fracture aperture during the E_s^2 sedimentary period showed similar distribution characteristics with that during the E_s^3 sedimentary period (Fig. 13d). That is, the E_s^2 sedimentary period was the key fracturing period to develop the FAZ in the DXFZ. Additionally, the fracture volume density and aperture during the E_s^1 sedimentary period showed similar developmental characteristics with that during the E_s^2 sedimentary period (Fig. 13e and f). The high fracture volume density (0.405−1.345 m^2/m^3) was primarily distributed along the EW-trending faults, near the NE-SW strike faults, and some FAZ, exhibiting strong rupturing and ability to producing more faults (small scale).

Comprehensively, three significant mechanic model of were summarized to analyze the fault accommodation zone in the DXFZ, a graben basin. For the parallel faults, the fault growth started from the respectively tensile strain regions (Fig. 14a). Then the outer extension branch could grow freely to the direction of the main compressive stress, and the inner extension branch was short. Consequently, the parallel fault accommodation zone (such as Xin 120 FAZ) was generated to regulating the redundant energy and deformation. For the cross-fault system, constrained by the

superposition of compressive strain on the inner side of the adjacent ends, the dielectric weaking generated (Fig. 14b). The outer tensile strain zone was conductive to the extension of the branch, and the two faults intersected by the shear extension along the strike. Then the convergent FAZ (Ying 66 and Ying 8 FAZ) and approach FAZ (Ying 26 FAZ) were developed to adjust the deformation and redundant strain energy. For the en echelon faults, influenced by the generation and connection of the compressive strain zone on the inner side, the internal medium was weakened and fragmented (Fig. 14c). Then a shear-compression zigzag fault was formed, cutting through the en echelon faults. Consequently, the overlap FAZ applied to regulate the rupturing energy and deformation among the en echelon faults was generated. For example, the Ying 26 FAZ was formed to adjust the strata deformation and release the redundant strain energy between the Ying 1 and Ying 31 faults. These produced models could be applied to analyze the formation process of the Dongxin fault zone.

5.6. Tectonic evolution model of the Dongxin fault zone

Since the deposition of the Kongdian Formation, the Shahejie sedimentary period was the key period for forming the Dongxin fault zone, especially different FAZ. Integrating the information and analyzed results of the paleo tectonic stress fields in the study area, three significant forming periods of the tectonic evolution of the DXFZ were distinguished as followed.
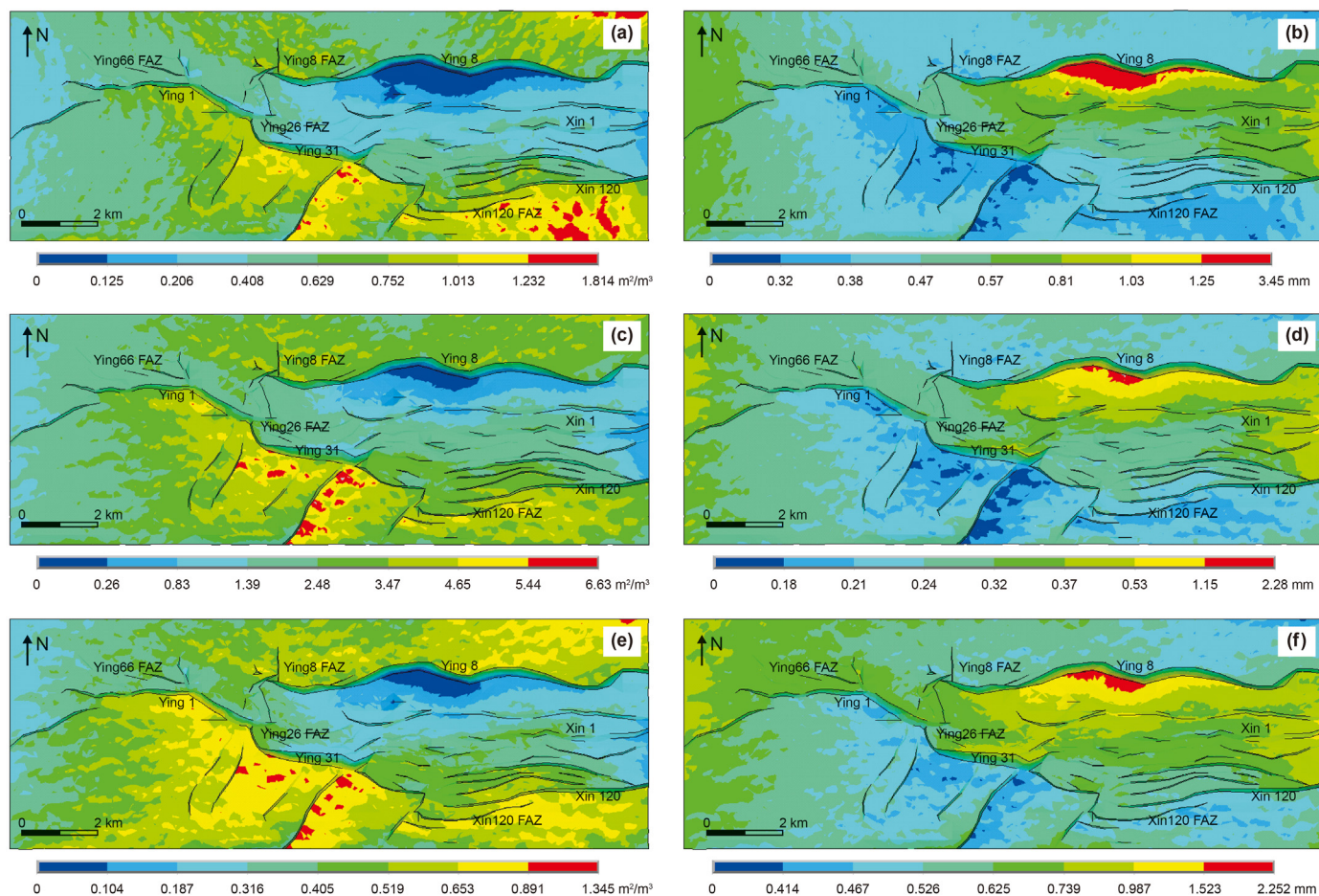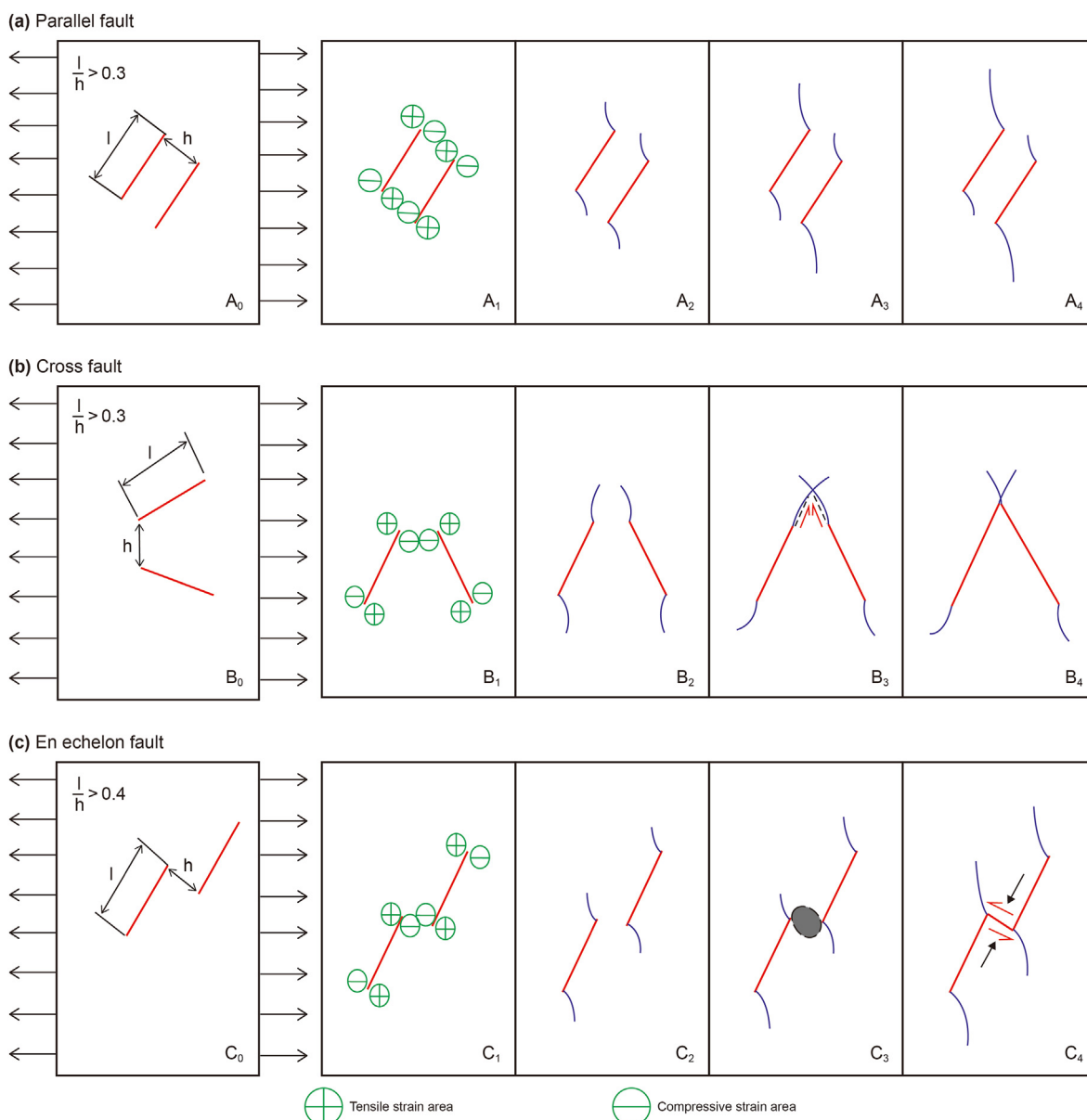
Fig. 13. The rupture characteristics during different periods in the study area. (a) is the fracture volume density during the Es^3 sedimentary period; (b) shows the fracture aperture during the Es^3 sedimentary period; (c) is the fracture volume density during the Es^2 sedimentary period; (d) shows the fracture aperture during the Es^2 sedimentary period; (e) is the fracture volume density during the Es^1 sedimentary period; (f) shows the fracture aperture during the Es^1 sedimentary period.

(1) During the early E_s^4 sedimentary period, according to the strong N-S extensional stress environment, the prototype of the EW-striking faults was generated (Fig. 15a). Consequently, during the middle-late E_s^4 sedimentary period, constrained by the N−S and E-W extensional stress environment ($\sigma_3 < \sigma_2 < 0$), several main faults of E-W striking were furtherly formed. Then the basic prototype of main faults in the DXFZ were generated, providing a framework of faults' formation in the DXFZ (Fig. 15b).

(2) During the E_s^3 sedimentary period, influenced by the strike-slip action of Tan-Lu fault zone, the NW-SE tensile stress and NE-SW dextral strike-slip stress were significant during the fault block-generating period in the Sag. The stress was primarily exhibited by the subsidence of the strata and the development of secondary normal faults. The large difference was identified in the stress, strain, and rupture distribution in various faults, especially in the nearly EW-trending faults of the east section. This stage was the key generation period for the prototype of the DXFZ, including the FAZ between large-scale faults (Fig. 15c).

(3) During the E_s^2 sedimentary period, the activity of the NE-SW trending faults was strengthened, and the central DXFZ area dropped and rifted. The EW-trending symmetric with opposite dipping normal faults were developed in the east section of the study area. Additionally, the NE-SW trending faults with large scale were furtherly developed, producing numerous small-medium scale normal faults. Emphatically, the junction area of two secondary normal faults were prone to be ruptured and formed the FAZ (convergent, approach, overlap, and parallel FAZ). The activity of the nearly EW- and NE-SW- trending faults were high and the activity of the NE-SE- and NS- trending faults was relatively low, exhibiting inherited characteristics from the development of fault accommodation zones during the E_s^3 sedimentary period (Fig. 15d). This stage was the significant period for the development of the DXFZ and the FAZ.

(4) During the E_s^1 sedimentary period, constrained by the combined stress of tension-torsional stress and diapir stress, the activity of the EW- and NE-SW- trending faults was enlarged. And the activity of the NW-SE- and NS- trending faults was high. The low-order faults were significantly influenced by the high activity of the tension-torsional and diapir upwelling motions along the secondary faults. The high-order faults in the DXFZ were characterized by the obvious fault depressions and strike-slip activity. Additionally, the NS-trending faults and several NW-strike faults (small-medium scale) were produced. The NE-SW- and nearly EW-trending faults indicated inherited characteristics from the development of fault accommodation zones during the E_s^2 sedimentary period. The developmental characteristics of the DXFZ was finally formed, and the FAZ regulating the

(a) Parallel fault

(b) Cross fault

(c) En echelon fault

⊕ Tensile strain area   ⊖ Compressive strain area

Fig. 14. The mechanic model and extension process of fault accommodation zone in different fault pattern. (a) was the parallel faults; (b) showed the cross faults; (c) referred to the en-echelon faults.

redundant strain energy and the deformation between two large-scale faults were finalized. This stage was the molded and formative period of the FAZ, the low-order faults, and the depression in the DXFZ (Fig. 15e).

6. Conclusions

In this manuscript, we presented a method for the numerical simulation of the tectonic evolution of fault accommodation zone in the Dongxin fault zone, graben basin. Combining the stress background with the similarity criterion, a tectonic physical simulation experiment was conduct to analyze the formation and development of the DXFZ (including the FAZ). Constrained by the tectonic stress environment and structural characteristics, a geomechanical model was established to obtain the paleo stress field and to analyze the generation and expansion of fault accommodation zones.

(1) The horizontal principal stress, the stress intensity, and elastic strain intensity could be applied to analyze the fault activity. Influenced by extensive torsion stress, combined with the Coulomb-Mohr rupture criterion, the fault strike was controlled by the planar shear stress and extensional stress, and the fault tendency was controlled by the tensile stress.

(2) Influenced by strike-slip action of Tan-Lu fault zone, the differential tension-torsional stress was the significant factor to control the formation and development of fault accommodation zones in DXFZ in graben basin in eastern China. Restricted by the combined stress of strong tension-torsional stress and diapir upwelling stress, the present complex structure of the DXFZ was formed with a little local compression. Consequently, the local rift, convergent FAZ, parallel FAZ, approach FAZ, and overlap FAZ were generated.
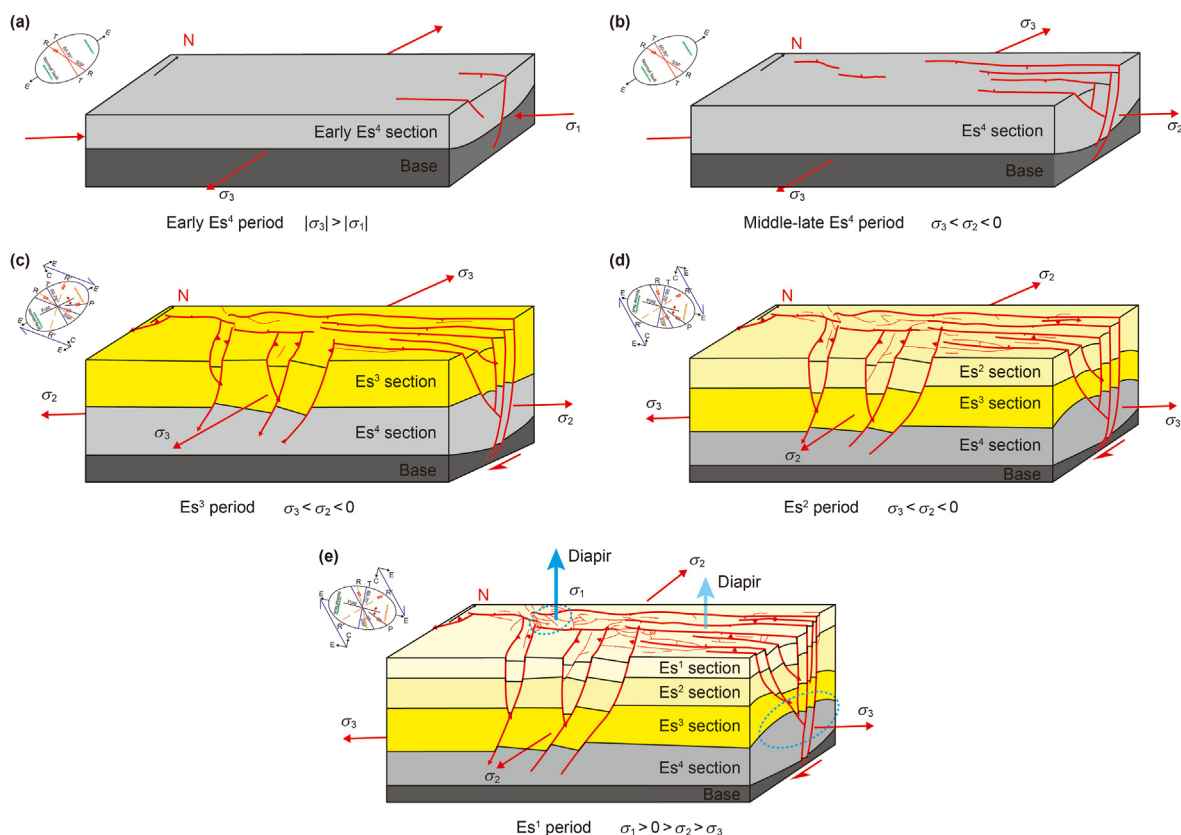
Fig. 15. The structural evolution model of the DXFZ. (a) is the early E_s^4 Formation sedimentary period; (b) shows the middle-late E_s^4 Formation sedimentary period; (c) is the E_s^3 Formation sedimentary period; (d) refers to the E_s^2 Formation sedimentary period; (e) shows the E_s^1 Formation sedimentary period, SSF-Simultaneous strike-slip fault.

(3) Influenced by the multiple complex tectonic activity, the DXFZ was generated with characteristics of extensional and strike-slip properties. Four significant tectonic evolution stages of the DXFZ were distinguished. During the E_s^4 sedimentary period, constrained by the N-S and E-W extensional stress environment ($\sigma3 < \sigma2 < 0$), the basic prototype of main faults in the DXFZ were generated, providing a framework of faults' formation in the DXFZ. During the E_s^3 sedimentary period, the large difference in the stress, strain, and rupture distribution in various faults were significant, and this stage was the key generation period for the prototype of the DXFZ. During the E_s^2 sedimentary period, the EW-trending symmetric with opposite dipping normal faults and the NE-SW trending faults with large scale were furtherly developed. The junction area of two secondary normal faults were prone to be ruptured, performing significant period for inheriting and developing characteristics of fault accommodation zones. During the E_s^1 sedimentary period, the high-order faults in the DXFZ exhibited the obvious fault depressions and strike-slip activity, and the fault accommodation zones were furtherly inherited and developed. This stage was the molded and formative period of the FAZ, the low-order faults, and the depression in the DXFZ.

Declaration of competing interest

The authors declare that they have no known competing financial interests or personal relationships that could have appeared to influence the work reported in this paper.

Acknowledgments

References

Andhumoudine, A.B., Nie, X., Zhou, Q., Yu, J., Kane, O.I., Jin, L., Djaroun, R.R., 2021. Investigation of coal elastic properties based on digital core technology and finite element method. Ager 5, 53—63. https://doi.org/10.46690/ager.2021.01.06.

Bellahsen, N., Leroy, S., Autin, J., Razin, P., d'Acremont, E., Sloan, H., Khanbari, K., 2013. Pre-existing oblique transfer zones and transfer/transform relationships in continental margins: new insights from the southeastern Gulf of Aden, Socotra Island, Yemen. Tectonophysics 607, 32—50. https://doi.org/10.1016/j.tecto.2013.07.036.

Bose, S., Mitra, S., 2010. Analog modeling of divergent and convergent transfer zones in listric normal fault systems. AAPG Bull. 94, 1425—1452. https://doi.org/10.1306/01051009164.

Bose, S., Mitra, S., 2014. Structural analysis of a salt-cored transfer zone in the south timbalier block 54, offshore gulf of Mexico: implications for restoration of salt-related extensional structures-structural analysis of south timbalier 54, offshore gulf of Mexico. AAPG Bull. 98, 825—849. https://doi.org/10.1306/08221313041.

Bosworth, W., 1985. Geometry of propagating continental rifts. Nature 316, 625—627. https://doi.org/10.1038/316625a0.

Bosworth, W., 1987. Off-axis volcanism in the Gregory rift, east Africa: implications for models of continental rifting. Geology 15, 397—400. https://doi.org/10.1130/0091-7613.

Cao, Y.C., Yuan, G.H., Li, X.Y., Wang, Y.Z., Xi, K.L., Wang, X.M., Jia, Z.Z., Yang, T., 2014. Characteristics and origin of abnormally high porosity zones in buried Paleogene clastic reservoirs in the Shengtuo area, Dongying Sag, East China. Petrol. Sci. 11, 346—362. https://doi.org/10.1007/s12182-014-0349-y.

Chen, D.X., Pang, X.Q., Jiang, Z.X., Zeng, J.H., Qiu, N.S., Li, M.W., 2009. Reservoir

characteristics and their effects on hydrocarbon accumulation in lacustrine turbidites in the Jiyang Super-depression, Bohai Bay Basin, China. Mar. Petrol. Geol. 26, 149—162. https://doi.org/10.1016/j.marpetgeo.2008.03.003.

Chorowicz, J., Benissa, M., 2016. Remote sensing and field analysis of the Palaeozoic structural style in NW Libya: the Qarqaf arch a paleo-transfer fault zone between the Ghadamis and Murzuq basins. J. Afr. Earth Sci. 123, 272—293. https://doi.org/10.1016/j.jafrearsci.2016.08.008.

Chu, R., Yan, D.P., Qiu, L., Wang, H.X., Wang, Q., 2023. Quantitative constraints on hydrocarbon vertical leakage: insights from underfilled fault-bound traps in the Bohai Bay Basin, China. Mar. Petrol. Geol. 149, 106078. https://doi.org/10.1016/j.marpetgeo.2022.106078.

Conti, A., Bigi, S., Cuffaro, M., Doglioni, C., Scrocca, D., Muccini, F., Bortoluzzi, G., 2017. Transfer zones in an oblique back-arc basin setting: insights from the Latium-Campania segmented margin (Tyrrhenian Sea). Tectonics 36, 78—107. https://doi.org/10.1002/2016TC004198.

Corti, G., Bonini, M., Mazzarini, F., Boccaletti, M., Innocenti, F., Manetti, P., Sokoutis, D., 2002. Magma-induced strain localization in centrifuge models of transfer zones. Tectonophysics 348, 205—218. https://doi.org/10.1016/S0040-1951(02)00063-X.

Dahlstrom, C.D.A., 1969. Balanced cross sections. Can. J. Earth Sci. 6, 743—757. https://doi.org/10.1139/e69-069.

Ding, Z.W., Li, X.F., Tang, Q.B., Jia, J.D., 2020. Study on correlation between fractal characteristics of pore distribution and strength of sandstone particles. Chin. J. Rock Mech. Eng. 39 (9), 1787—1796. https://doi.org/10.13722/j.cnki.jrme.2019.1555.

Faulds, J.E., Varga, R.J., 1998. The role of accommodation zones and transfer zones in the regional segmentation of extended terranes. Geol. Soc. Am. Spec. Pap. 323, 1—45. https://doi.org/10.1130/0-8137-2323-X.1.

Ferrill, D.A., Morris, A.P., 2001. Displacement gradient and deformation in normal fault systems. J. Struct. Geol. 23, 619—638. https://doi.org/10.1016/S0191-8141(00)00139-5.

Fossen, H., 2016. Structural Geology. Cambridge University Press, Cambridge, UK, pp. 480—481. https://doi.org/10.1017/CBO9780511777806.

Fossen, H., Rotevatn, A., 2016. Fault linkage and relay structures in extensional settings—a review. Earth Sci. Rev. 154, 14—28. https://doi.org/10.1016/j.earscirev.2015.11.014.

Fu, G., Yang, J.B., 2013. Sealing of matching between fault and caprock to oil-gas migration along faults: an example from middle and shallow strata in Nanpu depression. Earth Sci. J. China Univ. Geosci. 38 (4), 783—791. https://doi.org/10.3799/dqkx.2013.076.

Gawthorpe, R.L., Hurst, J.M., 1993. Transfer zones in extensional basins: their structural style and influence on drainage development and stratigraphy. J. Geol. Soc. LONDON 150, 1137—1152. https://doi.org/10.1144/gsjgs.150.6.1137.

Gibbs, A.D., 1984. Structural evolution of extensional basin margins. J. Geol. Soc. LONDON 141, 609—620. https://doi.org/10.1144/gsjgs.141.4.060.

Guo, P., Ren, D.S., Xue, Y.H., 2019. Simulation of multi-period tectonic stress fields and distribution prediction of tectonic fractures in tight gas reservoirs: a case study of the Tianhuan Depression in western Ordos Basin, China. Mar. Petrol. Geol. 109, 530—546. https://doi.org/10.1016/j.marpetgeo.2019.06.026.

Henaish, A., 2018. Soft-linkage transfer zones: insights from the northern eastern desert, Egypt. Mar. Petrol. Geol. 95, 265—275. https://doi.org/10.1016/j.marpetgeo.2018.05.005.

Hu, M., Jiang, H.J., Fu, G., Li, N., Chen, Y.J., 2016. Characterization of petroleum pooling patterns in dense flowerlike fault belts: taking the middle and shallow layers in Nanpu sag of Bohai basin as an example. Oil Gas Geol. 37 (4), 528—537. https://doi.org/10.11743/ogg20160409.

Hubbert, M.K., 1937. Theory of scale models as applied to the study of geologic structures. GSA Bulletin 48, 1459—1520. https://doi.org/10.1130/GSAB-48-1459.

Hunt, L., Reynolds, S., Hadley, S., Downton, J., Chopra, S., 2011. Causal fracture prediction: curvature, stress, and geomechanics. Lead. Edge 30, 1274—1286. https://doi.org/10.1190/1.3663400.

Islam, M.R., Hayashi, D., Kamruzzaman, A.B.M., 2009. Finite element modeling of stress distributions and problems for multi-slice longwall mining in Bangladesh, with special reference to the Barapukuria coal mine. Int. J. Coal Geol. 78, 91—109. https://doi.org/10.1016/j.coal.2008.10.006.

Jiu, K., Ding, W.L., Huang, W.H., You, S.G., Zhang, Y.Q., Zeng, W.T., 2013. Simulation of paleotectonic stress fields within Paleogene shale reservoirs and prediction of favorable zones for fracture development within the Zhanhua Depression, Bohai Bay Basin, east China. J. Petrol. Sci. Eng. 110, 119—131. https://doi.org/10.1016/j.petrol.2013.09.002.

Kimura, N., Matsuki, K., Nakama, S., Sato, T., 2003. Estimation of regional stress for heterogeneous rock mass. Journal mining and materials processing institute of Japan 119, 655—662. https://doi.org/10.2473/shigentosozai.119.655.

Konstantinovskaya, E.A., Harris, L.B., Poulin, J., Ivanov, G.M., 2007. Transfer zones and fault reactivation in inverted rift basins: insights from physical modelling. Tectonophysics 441, 1—26. https://doi.org/10.1016/j.tecto.2007.06.002.

Krantz, R.W., 1991. Measurements of friction coefficients and cohesion for faulting and fault reactivation in laboratory models using sand and sand mixtures. Tectonophysics 188, 203—207. https://doi.org/10.1016/0040-1951(91)90323-K.

Li, W., Wang, Z.B., Wang, G.Z., Xue, Y., Zhao, W.R., Zhang, X.Q., 2014. The Fault system and its fault sealing properties of the dome structure in dongying sag, east China. Geol. J. China Univ. 20, 93. https://doi.org/10.16108/j.issn1006-7493.2014.01.003.

Liu, J.S., Ding, W.L., Wang, R.Y., Yin, S., Yang, H.M., Gu, Y., 2017. Simulation of paleotectonic stress fields and quantitative prediction of multi-period fractures in

shale reservoirs: a case study of the Niutitang Formation in the Lower Cambrian in the Cen'gong block, South China. Mar. Petrol. Geol. 84, 289—310. https://doi.org/10.1016/j.marpetgeo.2017.04.004.

Liu, J.S., Ding, W.L., Dai, J.S., Wu, Z.H., Yang, H.M., 2018. Quantitative prediction of lower order faults based on the finite element method: a case study of the M35 fault block in the western Hanliu fault zone in the Gaoyou sag, East China. Tectonics 37, 3479—3499. https://doi.org/10.1029/2017TC004767.

Liu, J.S., Yang, H.M., Xu, K., Wang, Z.M., Liu, X.Y., Cui, L.J., Zhang, G.J., Liu, Y., 2022. Genetic mechanism of transfer zones in rift basins: insights from geomechanical models. GSA Bulletin 2, 1—17. https://doi.org/10.1130/B36151.1.

Lu, S.Q., Chen, G.J., Wu, K.Y., Feng, D.Y., 2013. Tectonic feature and evolution mechanism of central anticline belt of Dongying Sag, Bohai Bay Basin. Petroleum Geology & Experiment 35, 274—279. https://doi.org/10.11781/sysydz201303274.

Lu, Z.Y., Yang, S.C., Bai, Q.L., Zhang, S.W., Yang, K., Jing, Y.Y., 2019. Seismic identification of fault accommodation zones in Dongxin area. Oil Geophys. Prospect. 54, 433—446. https://doi.org/10.13810/j.cnki.issn.1000-7210.2019.02.023.

Ma, B.S., Qi, J.F., Ge, J.W., 2019. Development of two-phase transfer zones during multiphase rifting and their influence on sedimentation in the Baxian Sag, Bohai Bay Basin, northern China. Geol. Mag. 156, 1821—1838. https://doi.org/10.1017/S0016756819000190.

Mart, Y., Hall, J.K., Vachtman, D., 2018. Tiran straits: the transfer zone between the red sea and the gulf of elat and its tectonic significance. Mar. Petrol. Geol. 97, 105—112. https://doi.org/10.1016/j.marpetgeo.2018.06.028.

McClay, K.R., Dooley, T., Whitehouse, P., Mills, M., 2002. 4-D evolution of rift systems: insights from scaled physical models. AAPG Bull. 86, 935—959. https://doi.org/10.1306/61EEDBF2-173E-11D7-8645000102C1865D.

McKinnon, S.D., 2001. Analysis of stress measurements using a numerical model methodology. INT J ROCK MECH MIN 38, 699—709. https://doi.org/10.1016/S1365-1609(01)00037-5.

Mohammadnejad, T., Andrade, J.E., 2016. Numerical modeling of hydraulic fracture propagation, closure and reopening using XFEM with application to in-situ stress estimation. INT J NUMER ANAL MET 40, 2033—2060. https://doi.org/10.1002/nag.2512.

Morley, C.K., 1988. Variable extension in lake Tanganyika. Tectonics 7, 785—801. https://doi.org/10.1029/TC007i004p00785.

Morley, C.K., Nelson, R.A., Patton, T.L., Munn, S.G., 1990. Transfer zones in the East African rift system and their relevance to hydrocarbon exploration in rifts. AAPG Bull. 74, 1234—1253. https://doi.org/10.1306/0C9B2475-1710-11D7-8645000102C1865D.

Moustafa, A.R., 2002. Controls on the geometry of transfer zones in the Suez rift and northwest Red Sea: implications for the structural geometry of rift systems. AAPG Bull. 86, 979—1002. https://doi.org/10.1306/61EEDC06-173E-11D7-8645000102C1865D.

Moustafa, A.R., Khalil, S.M., 2017. Control of compressional transfer zones on syntectonic and post-tectonic sedimentation: implications for hydrocarbon exploration. J. Geol. Soc. LONDON 174, 336—352. https://doi.org/10.1144/jgs2016-030.

Paul, D., Mitra, S., 2013. Experimental models of transfer zones in rift systems. AAPG Bull. 97, 759—780. https://doi.org/10.1306/10161212105.

Peacock, D.C., Sanderson, D.J., 1994. Geometry and development of relay ramps in normal fault systems. AAPG Bull. 78, 147—165. https://doi.org/10.1306/BDFF9046-1718-11D7-8645000102C1865D.

Peacock, D.C.P., Knipe, R.J., Sanderson, D.J., 2000. Glossary of normal faults. J. Struct. Geol. 22, 291—305. https://doi.org/10.1016/S0191-8141(00)80102-9.

Peiro, A., Simón, J.L., Román-Berdiel, T., 2020. Fault relay zones evolving through distributed longitudinal fractures: the case of the Teruel graben system (Iberian Chain, Spain). J. Struct. Geol. 131, 103942. https://doi.org/10.1016/j.jsg.2019.103942.

Ren, Q.Q., Jin, Q., Feng, J.W., Li, M.P., 2019. Simulation of stress fields and quantitative prediction of fractures distribution in upper Ordovician biological limestone formation within Hetianhe field, Tarim Basin, NW China. J. Petrol. Sci. Eng. 173, 1236—1253. https://doi.org/10.1016/j.petrol.2018.10.081.

Ren, Q.Q., Jin, Q., Feng, J.W., Li, Z.Y., Du, H., 2020. Geomechanical models for the quantitatively prediction of multi-scale fracture distribution in carbonate reservoirs. J. Struct. Geol. 135, 104033. https://doi.org/10.1016/j.jsg.2020.104033.

Ren, Q.Q., Feng, J.W., Johnston, S., Zhao, L.B., 2021. The influence of argillaceous content in carbonate rocks on the 3D modeling and characterization of tectonic fracture parameters—example from the carboniferous and ordovician formations in the hetianhe gas field, Tarim Basin, NW China. J. Petrol. Sci. Eng. 203, 108668. https://doi.org/10.1016/j.petrol.2021.108668.

Soliva, R., Benedicto, A., 2004. A linkage criterion for segmented normal faults. J. Struct. Geol. 26, 2251—2267. https://doi.org/10.1016/j.jsg.2004.06.008.

Ter Borgh, M.M., Oldenhuis, R., Biermann, C., Smit, J.H.W., Sokoutis, D., 2011. The effects of basement ramps on deformation of the Prebetics (Spain): a combined field and analogue modelling study. Tectonophysics 502, 62—74. https://doi.org/10.1016/j.tecto.2010.04.013.

Tian, F., Jin, Q., Wang, D.P., Wang, J.X., Yang, Y., 2012. Fault accommodation zones and their controling effects on hydrocarbon distribution in yong 8 Fault block, dongying sag. Geol. J. China Univ. 18, 358. https://doi.org/10.16108/j.issn1006-7493.2012.02.011.

Tian, F., Yang, J.T., Cheng, M., Lei, Y.H., Zhang, L.K., Wang, X.X., Liu, X., 2016. Geometry, kinematics and dynamic characteristics of a compound transfer zone: the Dongying anticline, Bohai Bay Basin, eastern China. Open Geosci. 8, 612—629. https://doi.org/10.1515/geo-2016-0053.

Tong, H.M., Fan, C.W., Tong, C.X., 2015. Characteristics, types and genetic mechanism of Baodao transfer zone, Qiongdongnan Basin. Oil Gas Geol. 36, 897—905. https://doi.org/10.11743/ogg20150604.

Walsh, J.J., Watterson, J., 1991. Geometric and Kinematic Coherence and Scale Effects in Normal Fault Systems. Geological Society 56. Special Publications, London, pp. 193—203. https://doi.org/10.1144/GSL.SP.1991.056.01.1.

Wang, X.J., Li, Y.H., Hou, J.G., 2004. Two consideration in research of transition structures in extended region. Coal Geology of China 16, 4—6. https://doi.org/10.3969/j.issn.1674-1803.2004.02.002.

Wang, H.X., Lv, Y.F., Fu, X.F., Sun, Y.H., Wang, H.F., Li, P.H., 2013. Formation, evolution and reservoir-controlling mechanism of relay zone in rift basin. Geol. Sci. Technol. Inf. 32, 102—110. CNKI:SUN:DZKQ.0.2013-04-017.

Wang, G.H., Wang, H., Gan, H.J., Shi, Y., Zhao, Y.D., Chen, S.B., 2016a. Oil source and migration process in oblique transfer zone of Fushan Sag, northern South China Sea. J. Cent. S. Univ. 23, 654—668. https://doi.org/10.1007/s11771-016-3111-3.

Wang, J.H., Jiang, Z.X., Zhang, Y.F., Wei, X.J., Wang, H., Liu, S.Q., 2016b. Quantitative evaluation of the reservoir potential and controlling factors of semi-deep lacustrine tempestites in the Eocene Lijin Sag of the Bohai Bay Basin, East China. Mar. Petrol. Geol. 77, 262—279. https://doi.org/10.1016/j.marpetgeo.2016.05.006.

Wang, H.Y., Fu, X.F., Wang, H.X., Chen, M., Meng, L.D., Ping, G.D., 2020a. Research on the controlling effect of quantitative analysis and evaluation of fault activity on oil and gas accumulation in Qikou sag of Bohai Bay Basin. Acta Geol. Sin. 94 (10), 3062—3073. https://doi.org/10.19762/j.cnki.dizhixuebao.2020274.

Wang, Y.Z., Xie, Q.W., Cao, Y.C., Li, M.R., Wang, Y.S., Li, Y.Z., Wang, X., Xi, K.L., Mi, L.S., Guo, Y.C., Du, Y.J., 2020b. Influence of multistage oil emplacement on carbonate cementation in the eocene Shahejie Formation, dongying sag, Bohai Bay Basin, China. Mar. Petrol. Geol. 112, 104063. https://doi.org/10.1016/j.marpetgeo.2019.104063.

Wang, Q., Sun, Y.H., Zhang, W.F., Wang, Y.G., Cao, L.Z., Li, X.W., 2022. Structural characteristics and mechanism of the Hengshui accommodation zone in the southern Jizhong subbasin, Bohai Bay basin, China. Mar. Petrol. Geol. 138, 105558. https://doi.org/10.1016/j.marpetgeo.2022.105558.

Whittaker, A.C., Walker, A.S., 2015. Geomorphic constraints on fault throw rates and linkage times: examples from the Northern Gulf of Evia, Greece. J. Geophys. Res.-Earth 120, 137—158. https://doi.org/10.1002/2014JF003318.

Wu, Z.P., Zhang, L., Li, W., Gao, Y., Jia, H., 2012. Early Paleogene (E_k—E_s^{4x}) structure framework restoration of the dongying sag. Journal of China University of Petroleum 36, 13—19. https://doi.org/10.3969/j.issn.1673-5005.2012.01.003.

Xia, Q.Y., Wu, S.H., Feng, W.J., 2018. Quantitative evaluation of activities for contemporaneous reverse faults and associated folds: a case study of Huwan district in Northwestern margin of Junggar basin. Xinjing Pet. Geol. 39 (3), 296—303. https://doi.org/10.7657/XJPG20180306.

Xian, B.Z., Liu, J.P., Wang, J.H., Dong, Y.L., Li, Y.Z., Yan, Q., Liu, Y.L., 2018. Using of stratal slicing in delineating delta-turbidite systems in Eocene Dongying depression, Bohai Bay Basin: insights for the evolution of multi-source delta-turbidite systems in a fourth order sequence. J. Petrol. Sci. Eng. 168, 495—506. https://doi.org/10.1016/j.petrol.2018.05.043.

Xu, H., Wang, X.W., Yan, D.P., Qiu, Liang, 2018. Subsidence transition during the post-rift stage of the Dongpu Sag, Bohai Bay Basin, NE China: a new geodynamic model. J. Asian Earth Sci. 158, 186—199. https://doi.org/10.1016/j.jseaes.2018.03.001.

Yan, D.P., Xu, Y.B., Dong, Z.B., Qiu, L, Zhang, S., wells, Michael, 2016. Fault-related fold styles and progressions in fold-thrust belts: insights from sandbox modeling. J. Geophys. Res. Solid Earth 121 (3), 2087—2111. https://doi.org/10.1002/2015JB012397.

Yang, S.C., Bai, Q.L., Lu, Z.Y., Wang, Y., 2017. The forming mechanism simulation of Ying 26 transfer zone in Dongxin area. Journal of China University of Petroleum (Edition of Natural Science) 41, 25—33. https://doi.org/10.3969/j.issn.1673-5005.2017.01.003.

Yuan, B.H., Xu, L.G., Kang, N.S., Li, L., Zheng, L.H., Wang, G.Z., 2013. Related technical advances in petroleum seismogeology. Acta Pet. Sin. 34, 580—590. https://doi.org/10.7623/syxb201303025.

Zahid, M.A., Dong, C.M., Lin, C.Y., Gluyas, J., Jones, S., Zhang, X.G., Munawar, J.M., Ma, C.F., 2016. Sequence stratigraphy, sedimentary facies and reservoir quality of Es4s, southern slope of Dongying Depression, Bohai Bay Basin, East China. Mar. Petrol. Geol. 77, 448—470. https://doi.org/10.1016/j.marpetgeo.2016.06.026.

Ze, T., Alves, T.M., 2019. Impacts of data sampling on the interpretation of normal fault propagation and segment linkage. Tectonophysics 762, 79—96. https://doi.org/10.1016/j.tecto.2019.03.013.

Zhang, S.C., Zhang, L.Y., Zha, M., Zhu, R.F., Liu, Q., 2010. Control of pressure system development on reservoir formation in the dongying sag, shengli oilfield, east China. Petrol. Explor. Dev. 37, 289—296. https://doi.org/10.1016/S1876-3804(10)60033-X.

Zhang, Q., Zhu, X.M., Steel, R.J., Zhong, D., 2014. Variation and mechanisms of clastic reservoir quality in the Paleogene Shahejie Formation of the dongying sag, Bohai Bay Basin, China. Petrol. Sci. 11, 200—210. https://doi.org/10.1007/s12182-014-0333-6.

Zhang, X., Zhu, X., Lu, Z.Y., Lin, C.S., Wang, X., Pan, R., Geng, M.Y., Xue, Y., 2019. An early Eocene subaqueous fan system in the steep slope of lacustrine rift basins, Dongying Depression, Bohai Bay Basin, China: depositional character, evolution and geomorphology. J. Asian Earth Sci. 171, 28—45. https://doi.org/10.1016/j.jseaes.2018.11.018.

Zhao, S.J., Zhao, X.K., Yang, S.C., 2005. Similar analysis of geological structure physical model. Northwest. Geol. 38, 14—18. https://doi.org/10.3969/j.issn.1009-6248.2005.04.003.

Zhao, L, Li, Li, Zhang, H., 2014. Fault system's kinematic characteristics and dynamic mechanism during Early Cenozoic in Dongying sag. Journal of China University of Petroleum (Edition of Natural Science) 38, 18—24. https://doi.org/10.3969/j.issn.1673-5005.2014.03.003.